

ESLE

**ESD RECORD COPY**RETURN TO  
SCIENTIFIC & TECHNICAL INFORMATION DIVISION  
(ESTI), BUILDING 1211**ESD ACCESSION LIST**ESTI Call No. 63959Copy No. 1 of 1 cys.**Technical Report****456****Reflection Properties of Venus  
at 3.8 cm**R. P. Ingalls  
R. A. Brockelman  
J. V. Evans  
J. I. Levine  
G. H. Pettengill  
L. P. Rainville  
A. E. E. Rogers  
F. S. Weinstein

6 September 1968

Prepared under Electronic Systems Division Contract AF 19(628)-5167 by

**Lincoln Laboratory**

MASSACHUSETTS INSTITUTE OF TECHNOLOGY

Lexington, Massachusetts



AD681467

The work reported in this document was performed at Lincoln Laboratory, a center for research operated by Massachusetts Institute of Technology, with the support of the U.S. Air Force under Contract AF 19(628)-5167.

This report may be reproduced to satisfy needs of U.S. Government agencies.

This document has been approved for public release and sale; its distribution is unlimited.

Non-Lincoln Recipients

**PLEASE DO NOT RETURN**

Permission is given to destroy this document when it is no longer needed.

MASSACHUSETTS INSTITUTE OF TECHNOLOGY  
LINCOLN LABORATORY

REFLECTION PROPERTIES OF VENUS AT 3.8 cm

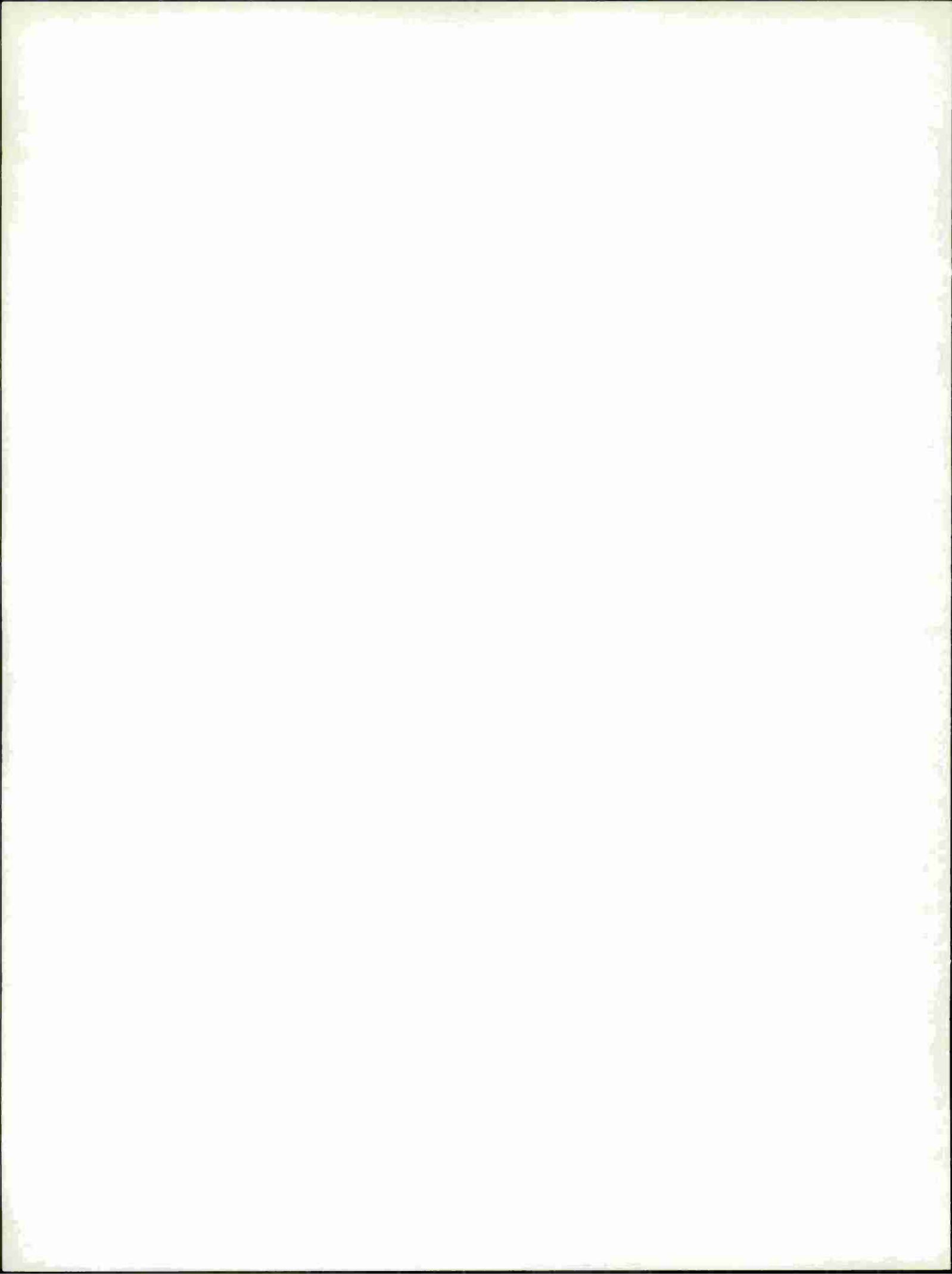
<i>R. P. INGALLS</i>	<i>G. H. PETTENGILL</i>
<i>R. A. BROCKELMAN</i>	<i>L. P. RAINVILLE</i>
<i>J. V. EVANS</i>	<i>A. E. E. ROGERS</i>
<i>J. I. LEVINE</i>	<i>F. S. WEINSTEIN</i>

TECHNICAL REPORT 456

6 SEPTEMBER 1968

LEXINGTON

MASSACHUSETTS



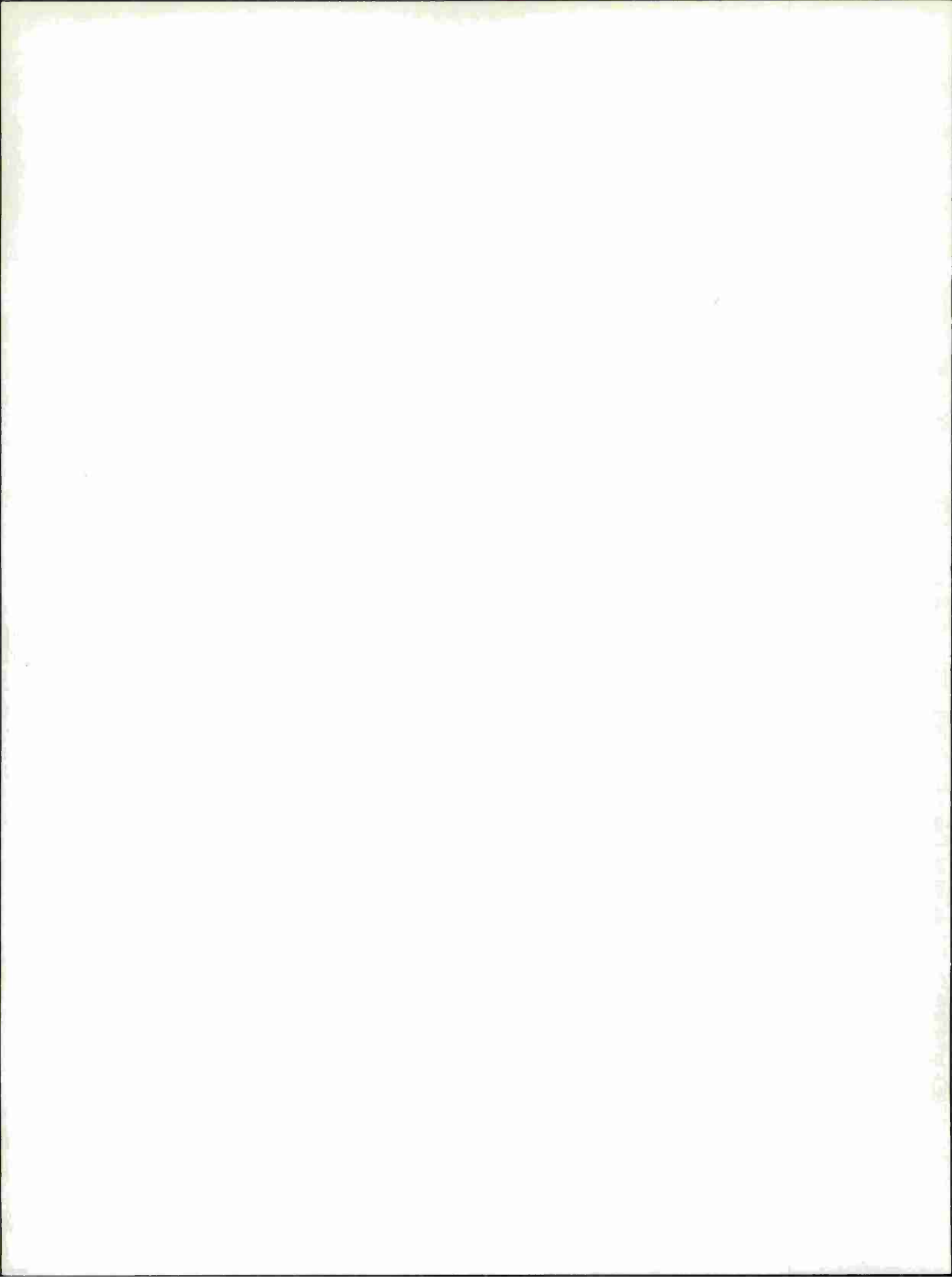
## ABSTRACT

During the fall of 1967, the M.I.T. Lincoln Laboratory Haystack radar was employed to study the scattering properties of the planet Venus at 3.8-cm wavelength. An increase in the transmitter power to 300 kW CW and a reduction in the system noise temperature to 60°K provided a considerable improvement in the radar performance compared with that available for earlier measurements. The frequency power spectra of the echoes were determined by digital Fourier analysis of the received signals. The total power in each spectrum was computed to yield the value for the radar cross section of Venus. These average 1.75 percent of the projected area of the disk, in good agreement with a reanalysis of results obtained in 1966.

The signal spectra have been averaged and employed to derive the angular scattering dependence  $P(\varphi)$  for waves reflected from a region near the center of the disk ( $0 < \varphi < 60^\circ$ ), where atmospheric refraction effects seem likely to be small. Comparison of this law with a law derived from similar measurements at 12.5-cm wavelength performed at the Jet Propulsion Laboratory (JPL) shows limb darkening, which is attributed to atmospheric absorption of the shorter wavelength signals. From the amount of limb darkening, the difference in the two-way atmospheric absorption at the two wavelengths is estimated to be  $5 \pm 1$  db. The radar cross section observed at 3.8 cm is lower than that at 12.5 cm by  $8 \pm 3$  db. Thus it is concluded that the one-way absorption of 3.8-cm microwaves by the atmosphere of Venus is at least 2.5 db and possibly more. This is significantly greater than can be accounted for by the recent U.S. and Soviet probe experiments, which imply an atmosphere of  $\text{CO}_2$  with surface pressure of 20 atmospheres. Either the pressure is considerably greater than this or other gases that are more effective microwave absorbers are present. The scattering behavior of the disk center, i.e., in a region where atmospheric refraction and absorption have not significantly altered the shape of the scattering law, has been compared with that at other wavelengths. It is concluded that Venus, like the moon, appears to be rougher at centimeter wavelengths than meter or decimeter wavelengths. However, for scales important in these measurements, i.e., over horizontal distances of the order of a few times the wavelength, the rms slopes found for Venus are of the order of  $1/\sqrt{2}$  times those found for the moon.

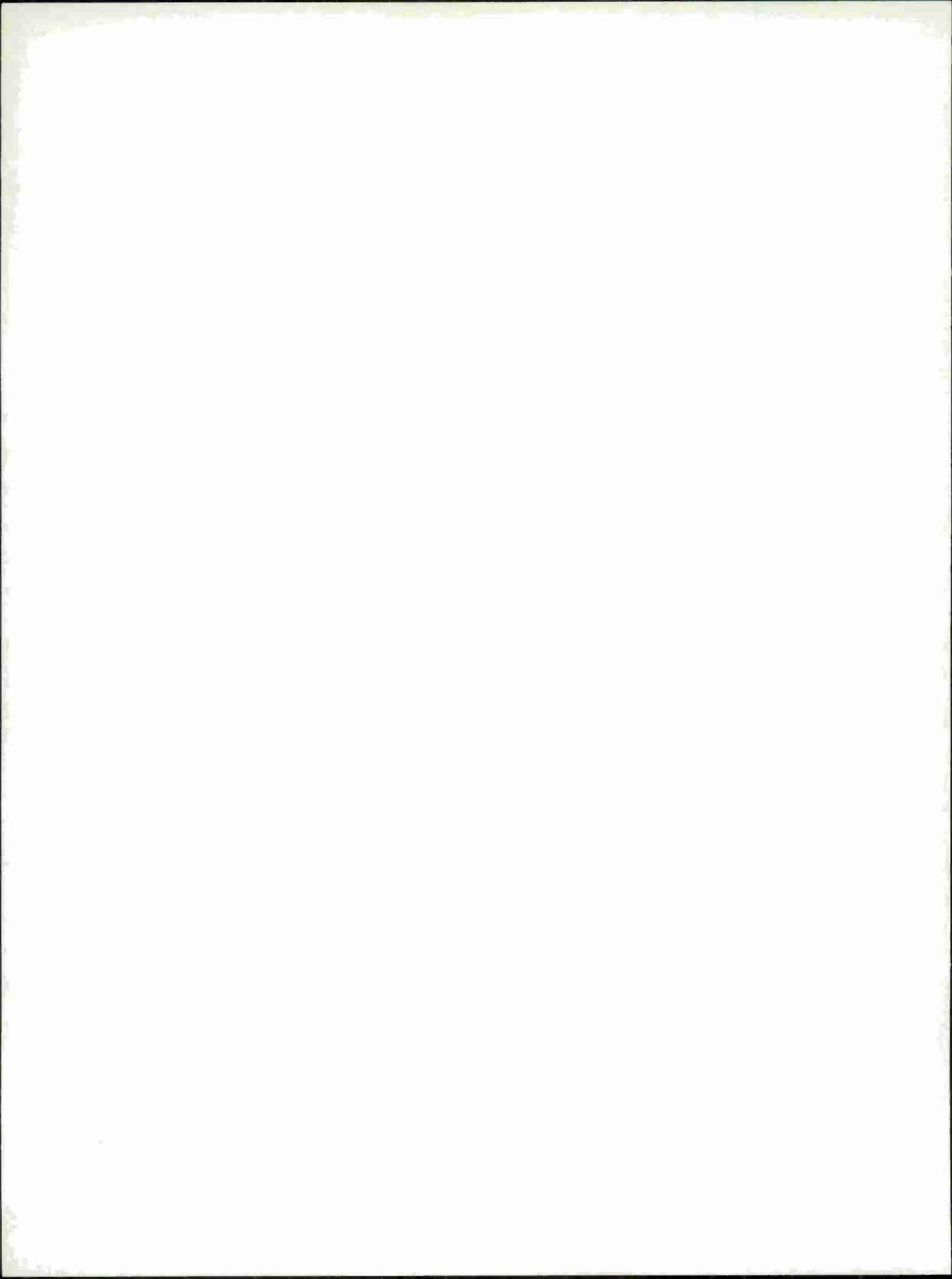
Delay-Doppler mapping experiments are reported which yielded a resolution of  $\sim 100 \times 100$  km. These show the existence of bright features and the locations of these are tabulated. The report closes with a discussion of the nature of these features. It is concluded that many, if not all, are rougher and denser than their environs and, in view of the general smoothness found elsewhere, are possibly young features.

Accepted for the Air Force  
Franklin C. Hudson  
Chief, Lincoln Laboratory Office



## CONTENTS

Abstract	iii
I. Introduction	1
II. Experimental System	1
A. General Characteristics	1
B. Frequency Control	3
C. Doppler and Range-Rate Tracking	4
D. Modulation and Timing Equipment	4
E. Data Interface to CDC 3300 Data Processing Computer	5
F. Computer Programs	5
III. Experimental Procedures	7
A. General	7
B. Hayford CW	7
C. Hayford Coded	9
D. Fourth Test of Relativity	9
E. CW Spectrum	10
IV. The Radar Cross Section	10
A. Reduction	10
B. Corrections	13
C. Accuracy	13
D. Results	16
V. The Angular Scattering Law	19
A. Mean Power Spectrum	19
B. Angular Power Spectrum $P(\varphi)$	21
C. Effects of Refraction in the Atmosphere of Venus	25
D. Absorption by the Atmosphere of Venus	28
E. Theoretical Behavior	31
VI. Mapping of Anomalous Scattering Regions	34
A. Introduction	34
B. Short Coded Pulse Observations	35
C. Spectrum Observations	39
D. Nature of the Features	44
E. Discussion	49
References	52





# REFLECTION PROPERTIES OF VENUS AT 3.8 CM

## I. INTRODUCTION

During a period of about 6 weeks centered on the 1967 Venus inferior conjunction, the Haystack Microwave Facility was employed as one element of a radar interferometer to map the brightness distribution over the disk of the planet. In addition, delay measurements of Venus were conducted as part of our overall program of determining planetary distances. Results pertaining to these particular experiments are published elsewhere.<sup>1-3</sup> As a consequence of the extensive radar coverage of the planet during this period and the high signal-to-noise ratio of the received signal, we have been able to analyze data from these two experiments for other purposes.

An extensive set of radar cross section measurements was available from the CW spectra obtained during the interferometer experiment. These same spectra and range delay data from both experiments were analyzed to obtain estimates of the scattering law and atmospheric attenuation of Venus at 3.8 cm. The features identified in radar maps and CW spectra from Venus were used to determine more precisely the rotation period of the planet. This report summarizes the results of these investigations.

In the section that follows, a general description is given of the radar system employed for these measurements. Section III reviews the experimental procedures employed for the four main experiments conducted during this period. The following three sections describe and discuss the experimental results obtained for (a) the radar cross section, (b) the scattering law and atmospheric absorption, (c) the mapping of the brightness distribution over the disk and the identification of anomalously scattering regions.

## II. EXPERIMENTAL SYSTEM

### A. General Characteristics

The radar experiments described in this report were performed with the 3.8-cm planetary radar at the Haystack Microwave Facility.<sup>4</sup> During the period of the 1967 Venus inferior conjunction, the receiving system was connected as an interferometer by using as a second antenna the 60-ft reflector at the Westford Communications Terminal.<sup>5</sup> The experiments to be described here were carried out using only the 120-ft Haystack antenna. The radar mapping results obtained using the interferometer configuration are described in Ref. 1 and will be referred to as the Hayford experiment.

The operating characteristics of the Haystack radar are listed in Table I. At 3.8 cm, the antenna has a gain of 66 db and a beamwidth of 0.07°. The narrow beamwidth requires that the

TABLE I  
HAYSTACK RADAR PARAMETERS  
(June - September 1967)

Frequency	7840 MHz
Wavelength $\lambda$	3.824 cm
Antenna diameter	120 ft
Antenna gain $G_t$	66.1 db
Antenna aperture $A_r$	26.9 db over $1 \text{ m}^2$
Beamwidth	$0.07^\circ$
Polarization	Transmit right circular Receive left circular
Average transmitter power $P_t$	150 to 350 kW
Typical system temperature $T_s$	$60^\circ\text{K}$
Modulation	CW or phase reversal code
Frequency standard	Hydrogen maser
System losses $L_s$	0.5 db

antenna be pointed extremely accurately and this is accomplished by generating pointing information in a Univac 490 computer from astronomical ephemerides.<sup>6</sup> Normally the computer directs the antenna at the apparent position of an object in the sky, and this would be correct for radar reception or radio astronomical observations of the planet. For experiments on Venus, however, during the transmission periods, the antenna must be commanded to "lead" the planet, i.e., the antenna must be directed at that point in the planetary orbit where the planet will be when the transmitted signals arrive. This was done automatically in the present observations by offsetting the antenna pointing by a small amount during transmission periods.

Figure 1 shows the arrangement of the principal components of the Haystack Radar. The transmitter employs a final stage consisting of two Varian VA-949AM klystrons and associated equipment. During the experiments reported here it was operated at average power levels of 150 to 350 kW. Since it is a CW transmitter, range measurement was accomplished by reversing the RF phase of the transmitter according to a pseudorandom sequence that could be recognized on reception.<sup>7</sup>

The receiver used for the experiments was a multiple superheterodyne with local oscillators controlled by the station frequency standard (Fig. 1). The preamplifier was a traveling wave ruby maser which was cooled to  $4.2^\circ\text{K}$  by liquid helium. The overall system temperature achieved during this period typically was  $60^\circ\text{K}$  when the antenna was directed against the sky at an elevation angle of the order of  $40^\circ$ . When the antenna was directed toward Venus at inferior conjunction, the system temperature rose to about  $70^\circ$ . The contribution of the receiver and its associated waveguide connections, combiner and horn to this total was about  $35^\circ\text{K}$ , the balance of the system temperature contribution being from radome loss, ground scatter, side lobes, atmospheric attenuation, and other causes.

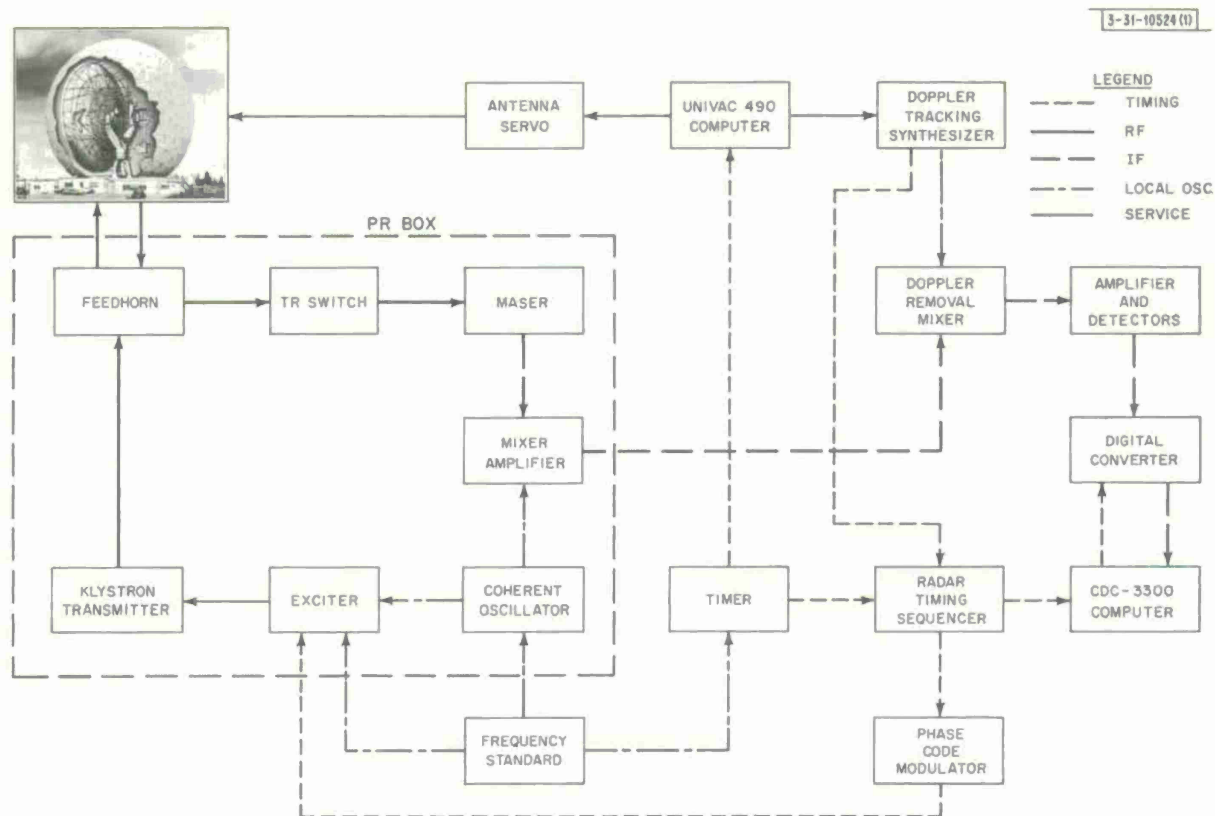


Fig. 1. Tuning and frequency control scheme in planetary radar at Haystack.

The liquid helium dewar holding the maser was malfunctioning during the report period and could only hold a charge for about 3 hours. An operational cycle of 1 hour charge followed by 3 hours observation therefore resulted. The first and last half hours of each of these observing periods were often contaminated by receiver gain instabilities. In treating the experimental results, the 3-hour groupings forced by this cycle were often summed together and the term "block" is here used to identify such run groups.

## B. Frequency Control

The basic element in the radar frequency control system was the station frequency standard. The operational standard was a Hewlett-Packard 107 BR 5-MHz quartz oscillator which was phase locked to a Varian H-10 hydrogen maser. All of the local oscillator and exciter signals were derived from this standard. The long term frequency stability was better than one part in  $10^{12}$  and the spectral purity of the radiated signal was known to be better than 0.05 Hz. The particular arrangement of the frequency control equipment used during the summer of 1967 was determined by the requirements of the Hayford experiment. Measurements of system phase stability and spectral purity are described in Ref. 1.

In the receiver, the first local oscillator frequency was fixed at 7710 MHz. The second local oscillator has a nominal value of 100 MHz but was electronically controlled to accomplish receiver Doppler frequency tuning. The third and fourth local oscillator frequencies were fixed at 28 and 2 MHz, respectively. In the CW measurements, a deliberate offset of the received signal frequency was accomplished by displacing either the 100-MHz or 2-MHz sources by a

known amount. This was done to avoid spurious signals and to provide an "image" reference spectrum of the noise in the system (see Sec. III-B).

### C. Doppler and Range-Rate Tracking

During the experiments the radar receiver was continuously tuned to compensate for the Doppler frequency shift of the received signal arising from the motion of the planet's center with respect to the observer. The ranging experiments required, in addition, a clock that was offset from that controlling the phase reversals in the transmitted waveform to compensate for the range-rate of the moving planet. The equipment used to track both the Doppler shift and range rate was under control of the Univac 490 pointing computer. The basic frequency control information was derived from the trial radar ephemeris (see Sec. II-A).

The Doppler frequency was removed by offsetting the second receiver local oscillator frequency (at 100 MHz) by the amount of the predicted Doppler shift. This local oscillator signal was generated by a digitally controlled frequency synthesizer (HP5100A), which could be changed in steps as fine as 0.1 Hz on command of the U490 pointing computer. Since the typical rate of change of frequency was less than 2 Hz per second, commands were transmitted from the computer to the synthesizer at a rate of 20 per second, and thus the receiver was always tuned to the nearest  $\pm 0.1$  Hz of the required value. The overall accuracy of this attempted compensation is determined by the basic ephemeris and knowledge of time. Subsequent spectrum analysis of the echoes was not attempted for a resolution finer than 1 Hz, and hence the frequency tuning system itself should not have produced significant spectral smearing or offset. Although the frequency of the synthesizer was stepped 20 times per second, phase discontinuities of the local oscillator were produced only by changes in the 1-kHz control digit, which occurred typically at 15-minute intervals.

In designing the equipment used to generate the range rate offset clock signal, advantage was taken of the fact that the fractional frequency offset required is identical to the ratio of the Doppler frequency shift to the carrier frequency. Thus 100 MHz was subtracted from the second local oscillator frequency to generate the "Doppler" frequency offset. This was then divided by 7840 (i.e., the carrier frequency in MHz) and applied as a single-sideband modulation to the standard 1-MHz clock signal preserving sign as well as magnitude. This compensated clock signal was then employed to control the sampling of the echo, i.e., to generate a receiver time base on which the echo would appear to be stationary. The actual implementation of this scheme was in fact more complex than described above, since it was required to work over a wide range of Doppler frequencies and operate smoothly through the zero Doppler shift region. In operation it was merely necessary for the U490 computer to program the 100-MHz local oscillator to the correct frequency in order to compensate simultaneously the Doppler and range-rate variations.

### D. Modulation and Timing Equipment

Timing and modulation signals for the various experiments were generated by a special radar sequencer. All experiments were timed to start on a selected even minute and the duration of the transmit period was made equal to round trip time delay to the planet. During this period the antenna pointing was made to lead the apparent position, and in the ranging experiments pseudorandom phase-reversal modulation was applied to the transmitter. The end of the round trip time was established to the nearest 1  $\mu$ sec using a digital clock which commenced running on the minute mark. The preset entries for this clock were obtained from a printed ephemeris.



After the transmit period had elapsed there was a receive period timed to be of equal duration, the combination constituting a "run." In the receive period the antenna was pointed at the apparent position of the planet and the Doppler shift of the receiver was compensated automatically. Samples of the signal were taken using analog to digital (A/D) converters and these were processed by the CDC 3300 computer. The sequencer provided signals to start and stop the processing and to control the timing of the analog-to-digital converters. For ranging experiments this conversion was performed at a rate governed by the range-rate offset clock. Since the details of timing for each experiment varied, these are discussed in Sec. III under Experimental Procedures.

#### E. Data Interface to CDC 3300 Data Processing Computer

The final intermediate frequency of the radar receiver was 2 MHz. The analog signals at 2 MHz were band limited to reduce the dynamic range requirements of signal processing. This signal was translated to a 0-Hz intermediate frequency by two identical balanced mixers (or "phase detectors") fed by quadrature reference signals at or near 2 MHz. The resulting pair of quadrature video signals represents orthogonal components of the complex signal. (During the Hayford experiments, a second analog signal channel was processed simultaneously.) These video signals were filtered by a pair of identical low pass filters, and this is equivalent in its effect to that of a single bandpass filter of the same half width at IF. The low pass filters used in the spectral measurements were 5-pole units providing a sharp cutoff above 250 Hz. The filters used in coded range measurements were filters matched to a pulse equal in length to the basic interval (baud) employed in the code sequence.

The filtered analog signals were amplified and then sampled simultaneously by analog "sample-and-hold," circuits. The stored voltages were then sequentially measured by an 8-bit analog-to-digital converter. The encoded outputs were placed in proper format and transmitted directly to the lower 16,000 word memory section of the CDC 3300 computer. These operations were always under timing control of the radar sequencer, which generated start and stop commands and supplied range-rate offset sampling pulses for ranging measurements. The interface equipment directly controls the location in core memory for each data word and periodically communicates control information (and time if required) to the computer program via a standard computer communication channel in order to synchronize the cycling of the program to the radar timing.

#### F. Computer Programs

All of the programs used for processing the radar signals in real-time (i.e., on receipt) by the experiments covered in this report were written for the Control Data Corporation 3300 computer system. This computer has an effective cycle time of about  $1.4 \mu\text{sec}$ , a word size of 24 bits and 32,000 words of directly addressable core storage.

Our objective in writing these programs was to accomplish as much of the desired analysis of the digital samples accepted from the radar as possible during their arrival. The extent to which any analysis can be carried out while receiving data samples is primarily a function of their input rate, the speed of the computer and the efficiency of the processing program. For two of the experiments, namely the Hayford Coded and the Fourth Test measurements (Secs. III-C and -D), the transmitted waveform was phase coded to obtain range resolution. For these two cases, the real-time program performed the demodulation of the received signal by effectively

cross correlating the signal with a replica of its transmitted waveform. This was accomplished in the computer, in practice, by executing a sequence of additions and subtractions of the data samples in a pattern identical to the sequence of phase shifts imposed on the transmission.

In all of the experiments, digital frequency filtering was performed at some point in the data analysis. In the Hayford CW and CW Spectrum measurements (Secs. III-B and -E, respectively), this was accomplished in real-time, i.e., during the receive period of the radar system cycle. In the Fourth Test experiment (Sec. III-D), frequency analysis for each run was performed during the transmit period of the succeeding run. This was necessary for this experiment since the high input data rate restricted the receive period processing to demodulation of the coded signal. These decoded samples were then recorded on magnetic tape for use by the spectral processing phase of the program.

The Hayford Coded real-time program (Sec. III-C) also produced a record of the decoded samples but in this case the frequency analysis was accomplished by an "off line" program. In all cases, this computation of power spectra was accomplished by performing a discrete Fourier transformation of the time domain samples using an algorithm for fast Fourier transform developed by Cooley and Tukey.<sup>8,9</sup> The time required to execute this algorithm is proportional to  $N \log N$  where  $N$  is the number of spectrum points (normally equal to the number of data samples). The routine is especially fast where  $N$  is some power of 2. Consequently for all of the real time programs  $N$  was chosen as an exact power of 2. Table II summarizes the operating statistics of the real-time programs.

TABLE II					
REAL-TIME COMPUTER PROGRAMS					
A. CODED PULSE PROGRAMS					
Experiment	Effective Pulse Length (μsec)	Sample Delay Interval (μsec)	Number of Delays Decoded	Data Input Rate (24-bit words/sec)	Percent of Processing Capacity
Fourth Test	60	30	32	66,667	99
Hayford Coded	500	500	62*	16,000	90
B. SPECTRAL PROGRAMS					
Experiment	Frequency Spacing (Hz)	Number of Frequencies	Data Input Rate (24-bit words/sec)	Percent of Processing Capacity	
Hayford CW	1.0	1024*	2048	70	
CW Spectrum	8.0 – 1.0	128 – 1024	256 – 2048	60 – 80	
Fourth Test	1.033	64	NA†	85	

\* Hayford was a 2-station interferometric experiment. For this report we consider only one signal or 31 delays and 512 frequencies.

† Spectral processing performed during subsequent transmit period.

### III. EXPERIMENTAL PROCEDURES

#### A. General

This report presents results obtained from several experimental programs that required different operating procedures which are reviewed below. In general, the experiments had been designed with given primary objectives in mind and in all cases were not ideal for the measurements discussed here. For the purpose of this report, the following names will be used to identify the primary experiments:

- (1) Hayford CW<sup>1</sup>. The Venus X-band CW radar interferometer experiment performed with the Haystack and Westford Communications Terminal antennas.
- (2) Hayford Coded<sup>1</sup>. The Venus range-coded radar interferometer measurements performed in conjunction with the Hayford CW experiment.
- (3) Fourth Test Ranging<sup>3</sup>. The experiment designed to directly test the theory of General Relativity by radar planetary ranging. Some of these observations were conducted using a code with a 60- $\mu$ sec baud length and as such were suitable also for (ambiguous) mapping of Venus.
- (4) CW Spectrum. A monostatic spectral analysis experiment specifically designed for CW spectral and radar cross section measurements on Venus and Mercury.

The Hayford CW experiment has been the primary source of data presented in this report and the experimental procedures used for the others were quite similar.

#### B. Hayford CW

The primary purpose of the Hayford experiment was radar mapping of the surface of Venus by combining Doppler frequency resolution and interferometric techniques to resolve areas on the surface. A CW signal was transmitted for a period approximately equal to the round trip delay interval. During the receive interval, the planetary echo was received at both Haystack and Westford and a real-time spectral analysis of the signals was performed by the CDC 3300 data processing computer. The data of interest to this report are the average power spectra derived from the Haystack signals.

The timing of each radar run was determined by the requirements of the interferometer experiment. The commencement of both the run and data processing had to be at predetermined clock times and it was also necessary to allow a finite amount of time to convert from transmitting to receiving. One consequence was that the total integration time available per run was somewhat less than the round trip delay time. In a typical run such as 22804\* on 16 August 1967, the round trip delay time was 312.345 seconds and the resulting integration time was 265 seconds.

During the transmit period, the operator attempted to maintain the transmitter at constant power. However, for the purposes of the primary experiment, it was more important to maintain a continuous cycle of runs than to maintain constant power. As a consequence, there were a considerable number of runs during which the transmitter power varied as the voltage was being raised, or when safety circuits removed the drive signal. We have attempted to identify such

---

\* A 5-digit "run" numbering system was used to identify the day number of the year (first three digits) and to assign 2-digit serial numbers to the runs on that day (last two digits). Generally, Venus experiments started daily with the serial number 01, and where a new block of data began (see Sec. II-B) a new series would be started at say 11, 21, or 31.



runs and eliminate them from the data from which the radar cross section has been determined (Sec. IV).

The system temperature was measured at the conclusion of each run by injecting into the receiver terminals a known amount of noise and observing the increase in the mean level at the output. This method of calibration introduces uncertainty during the conditions of receiver instability that were experienced at the beginning and end of the liquid helium fill and under adverse weather conditions. The receiver system temperature was found to be stable most of the time, except, of course, for the variation with elevation angle introduced by atmospheric extinction (see Sec. IV-B).

The predicted Doppler shift was compensated as outlined above. The 2-MHz IF signal was band-limited by an 18-kHz wide filter whose passband was essentially flat over the center portion.

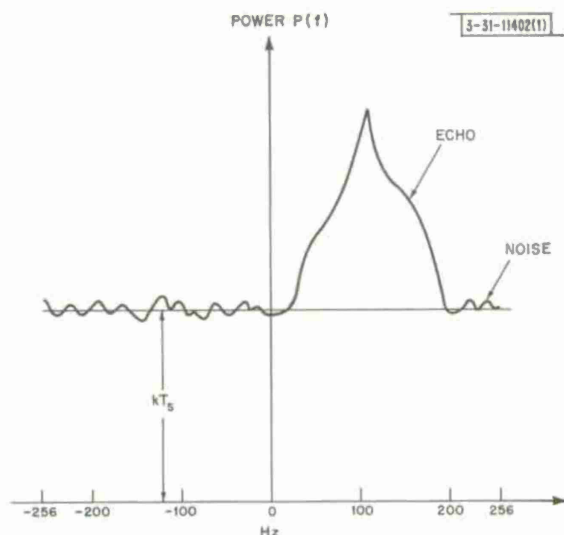


Fig. 2. Schematic diagram of receiver output for CW operations following spectral analysis processing in computer.

For the Hayford CW experiment the center of the echo was arranged to appear at a frequency of 2,000,100 Hz. Phase detectors translated two quadrature components of this signal to video where low pass filters then limited the total bandwidth effectively to  $\pm 250$  Hz. There was deliberate aliasing of noise components by the subsequent sampling. This produced a virtually flat noise baseline in the processed data, making the removal of the noise contribution from the spectrum rather straightforward. Since the limb-to-limb Doppler spread of the signals (except for the first few days of operation) was less than 200 Hz, the signal spectrum was located within a band extending from 0 to +200 Hz, centered at +100 Hz. Thus the region of the spectrum extending from 0 to -200 Hz could be used to establish the level of the noise baseline. The form of the spectrum is shown in Fig. 2 with

the Venus echo centered at +100 Hz and the symmetrical noise reference baseline (see Sec. IV).

As described above, the analog data was sampled and digitally encoded for computer processing. The intersample period used for the pair of quadrature signal components was 1953  $\mu$ sec corresponding to a sampling rate and frequency coverage of 512 Hz (512.03277). The encoded data was transferred to the CDC 3300 data processing computer, where a complex Fourier spectral analysis for 512 points (1 second) produced complex amplitude spectra with a 1-Hz frequency resolution.<sup>1</sup> This program<sup>8</sup> was based on the direct discrete Fourier transform algorithm developed by Cooley and Tukey,<sup>9</sup> and did not apply any weighting to reduce sidelobes. Hence the synthesized "filter" characteristic has a  $(\sin x/x)^2$  power response with 1-Hz effective bandwidth per filter. Features seen in the spectra of the signals seem to have been resolved, that is to say they were found to extend over several adjacent filters. Therefore it is believed that the sidelobes in this response should not introduce spurious effects. The series of complex amplitude spectra were recorded on magnetic tape for later analysis. In the example of run 22804, there were 265 such spectra, each representing 1 second of coherent integration performed during this run. These stored complex spectra were later (i.e., in post real-time) squared and



summed to generate average power spectra for each run. These average power spectra provided the source for the results described in Secs. IV and V and were one source for those of Sec. VII.

### C. Hayford Coded

The primary purpose of this experiment was radar mapping of the surface of Venus using a combination of delay resolution, frequency resolution and interferometric techniques to resolve areas of the surface.<sup>1</sup> The transmitted signal was modulated by reversing the phase ( $180^\circ$ ) according to a 31-element pseudorandom shift-register sequence code.<sup>7</sup> The baud or basic pulse width was  $500\mu\text{sec}$  and the resulting unambiguous code length  $15.5\text{ msec}$ . This may be compared with the  $40.7\text{-msec}$  radar depth of Venus. The energy from delay depths beyond  $15\text{ msec}$  was folded onto the initial returns, but because of the rapid fall-off of the scattered energy with incremental range delay, this did not cause any difficulty in the primary mapping experiment.

The operational procedure employed was basically the same as that described for the Hayford CW experiments with the exception that, because the transmitted signal was phase-coded, the computer processing was different. The signal was not frequency offset before processing. The video signals were smoothed by filters matched to  $500\text{-}\mu\text{sec}$  rectangular pulses, and sampled at  $500\text{-}\mu\text{sec}$  intervals. The computer removed the code by weighting 31 adjacent samples by  $+1$  or  $-1$  and summing. This operation was repeated each time a new sample was received. Subsequent spectral analysis of the successive sums produced an (ambiguous) delay-Doppler map containing 31 delay elements, each  $500\text{ }\mu\text{sec}$  in width, times 64 frequency elements, each approximately  $1\text{ Hz}$  wide.

The delay-Doppler maps obtained during these experiments were summed with respect to frequency to obtain a plot of echo power vs incremental delay. These profiles were used to estimate planetary scattering law (Sec. V). The first two  $500\text{-}\mu\text{sec}$  range boxes were arranged to precede the echo (i.e., the leading edge of the Venus echo appeared in box 3), thereby providing a noise calibration. Thus the delay depth coverage was restricted to less than  $15\text{ msec}$  and the noise reference boxes were contaminated by weak but nevertheless finite planetary returns, owing to foldover.

### D. Fourth Test of Relativity

The Haystack radar was used extensively in range delay measurements of Venus and Mercury during 1966 and 1967, in order to refine the elements of their orbits (and earth) and test the General Theory of Relativity.<sup>3</sup> The experimental results obtained during the period of the 1967 Venus inferior conjunction in the course of this program were used to estimate the planetary scattering characteristics near the subradar point. The ranging technique employed pseudorandom phase reversal coding with computer demodulation and processing, and was therefore similar to the Hayford coded experiment except that a 63-element code with a  $60\text{-}\mu\text{sec}$  baud length were employed. These provided an unambiguous range delay coverage of  $3780\mu\text{sec}$ . The video signals were smoothed by filters matched to a  $60\text{-}\mu\text{sec}$  rectangular pulse (i.e., the baud length). Because of the requirements of the primary experiment and the limited data processing capabilities of the CDC 3300 computer, only a portion of the time base was examined. The uncoding of the signals was carried out to provide voltage sums for 32 range boxes. The spacing between adjacent sums was  $30\mu\text{sec}$  thus providing a depth of coverage of  $960\mu\text{sec}$ . As with the Hayford coded data, signals returned from deeper in the planet were folded onto the wanted portion. The echo power falls off so rapidly with incremental delay, however, that this "self noise" can be

tolerated for the purposes of the range measurements. The foldover problem served to prevent the establishment of an accurate noise baseline. A second problem associated with establishing a baseline was the presence of small but consistent end-effects resulting from the particular way the pseudorandom sequence modulation was decoded. This end-effect caused the various range boxes to contain slightly differing levels even in the absence of an echo.

The processing produced a delay-Doppler map having 32 delay elements, each 30  $\mu$ sec in width, times 64 frequency elements, each approximately 1-Hz wide. The first four range boxes served as a noise baseline reference with the leading edge of the Venus return usually placed in box 5 or 6. These delay-Doppler maps could be transformed to generate an (ambiguous) map of the Venus reflectivity near the subradar point with a finer resolution than provided by the 500- $\mu$ sec Hayford coded data (see Sec. VI). The delay-Doppler data was summed across frequency to obtain range delay profiles of the planetary return near the leading edge (see Sec. V).

### E. CW Spectrum

The primary purpose of this experiment was to measure the planetary echo during periods of relatively weak signal-to-noise ratio and to obtain estimates of radar cross section and signal spectra. The spectra obtained were generally noisier and of poorer resolution than those generated by the Hayford CW experiment. The experimental procedure was almost identical to the Hayford arrangement but had the complications caused by the interferometric system removed. A CW signal was transmitted for a period of one round trip delay interval followed by a similar receive period. The actual time for which the echo signal was recorded was usually about 45 seconds less than the round trip delay time.

The average power spectrum of the received signal was computed in real-time. The frequency coverage of the spectral analysis was about 1024 Hz, the intersampling period being 977  $\mu$ sec for the pair of complex components. Equivalent filter resolutions of 1 or 8 Hz were used at different times depending upon the signal-to-noise ratio. The planetary signal was displaced to appear centered at +160 Hz so that the negative side of the spectrum was available as a symmetrical noise reference (see Sec. IV).

## IV. THE RADAR CROSS SECTION

### A. Reduction

Hayford CW spectra were obtained for 165 runs during the period of 27 July to 13 September 1967. These runs were grouped into 23 blocks of data, each block covering a 4-hour time interval. The blocks were used to generate absolute spectra and to compute the radar cross section. Additional estimates of the radar cross section have been obtained from CW spectrum runs made during the period April to July 1967.

The cross section of Venus  $\sigma$  was computed from the radar equation

$$\sigma = \frac{(4\pi)^2 R^4 P_r}{P_t G_t A_r L} \quad (1)$$

using the parameters listed in Table I. Here  $R$  is the distance to Venus and  $L$  is a composite loss transmission factor made up of transmission line loss, elevation angle corrections, and weather attenuation (see Sec. IV-B). In order to determine the received power  $P_r$ , the average power spectra were read from a previously prepared magnetic tape. These spectra spanned a

frequency interval of 512 Hz, i.e., from -256 to +256 Hz. The echo appears at positive frequencies centered at +100 Hz and is superimposed on a noise background as illustrated in Fig. 2. The noise level on the negative side of the spectrum was relatively flat and had a mean value  $\bar{P}_n$  watts/Hz related to the actual system temperature  $T_S$  by

$$\bar{P}_n = kT_S \quad (2)$$

where  $k$  is Boltzmann's constant.

The spectra were scaled in temperature by using this relationship and the recorded system temperature. The signal power  $P_r$  was computed from the spectrum by summing the temperature contributions of the filters over a range equal to the limb-to-limb Doppler spread

$$P_r = kB \left[ \sum_m T_f(f) - \sum_m T_n(-f) \right] \quad (3)$$

where  $m$  is the number of filters employed in the sum,  $T_f(f)$  the temperature assigned to the filters (centered on +100 Hz) containing signal and noise, and  $T_n(-f)$  the temperature assigned to the filters centered on -100 Hz containing only noise. The noise subtraction [Eq. (3)] depends for its accuracy on the fact that the weighting imposed by the low pass filter will be the same for positive and negative frequencies, while the gain of the receiver prior to the conversion to video is essentially constant over the narrow frequency interval examined here. However, the amount of noise in the left and right halves of the spectrum (Fig. 1) is only the same on a statistical basis and thus the subtraction [Eq. (3)] does introduce a slight amount of uncertainty in  $P_r$  (see Sec. IV-C).

The radar range was computed from the ephemeris round trip delay time

$$R = ct_R/2 \quad (4)$$

where  $c$  = velocity of light and  $t_R$  = round trip delay time. The computer was employed to calculate  $\sigma$  using the following modification of Eq. (1).

$$\sigma = (\pi^2 c^4 k) \left( \frac{B}{G_t A_r L_s} \right) \left( \frac{t_R^4}{P_t L_E L_V} \right) \left[ \sum_m T_f(f) - \sum_m T_n(-f) \right] \quad (5)$$

where  $L_E$  is the extinction loss (see Sec. IV-B) and  $L_V$  any additional loss attributable to adverse local weather (see Sec. IV-B). The other parameters are again specified in Table I. Equation (5) separates into four factors: the first is a constant; the second contains only parameters that were assumed to be invariant during the course of the experiment; the third contains parameters that varied from run-to-run, and the values of these were entered into the program by punched cards; and the fourth was the temperature sum obtained by adding the signal temperature contributions over the predicted limb-to-limb spread. A discussion of the errors involved in this computation is included in Sec. IV-C.

The radar cross section values obtained in terms of percentage of projected area of Venus (taken as  $1.17 \times 10^{12} \text{ m}^2$ ) for each block of data are summarized in Table III, and discussed later in this section. The reduced echo spectra were averaged over each block and, together with the relevant scaling information, were recorded on magnetic tape for further analysis.

TABLE III					
HAYFORD CW MEASUREMENTS OF RADAR CROSS SECTION $\sigma$					
Block No.	Date (1967)	Time (GMT)		No. of Runs	Percent Cross Section
		First	Last		
208-1	27 July	1743	1953	7	1.86
214-1	2 Aug	1435	1628	5	1.80
214-2		1755	1959	4	1.82
215-1	3 Aug	1404	1507	5	1.92
222-1	10 Aug	1343	1605	10	1.77
222-2	10 Aug	1705	2008	12	1.81
228-1	16 Aug	1346	1550	12	1.72
228-2	16 Aug	1931	2031	6	1.61
229-1	17 Aug	1309	1536	10	1.65
229-2	17 Aug	1742	2014	10	1.64
235-1	23 Aug	1655	1834	9	1.68
235-2	23 Aug	1939	2134	6	1.79
237-1	25 Aug	1745	1756	2	1.79
241-1	29 Aug	1553	1800	8	1.78
241-2	29 Aug	1921	2128	7	1.62
242-1	30 Aug	1447	1704	9	1.72
242-2	30 Aug	1831	1926	6	1.59
243-1	31 Aug	1410	—	1	1.74
249-1	6 Sept	1425	1458	3	1.85
249-2	6 Sept	1735	1937	9	1.70
250-1	7 Sept	1837	2023	10	1.74
256-1	13 Sept	1438	1514	4	1.71
256-2	13 Sept	1820	2024	8	1.62
					mean = 1.74%

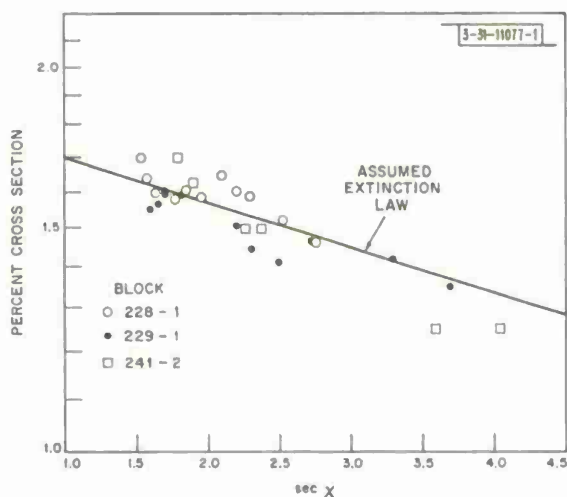


Fig. 3. Variation of radar cross section with local zenith angle  $\chi$  for three operating periods. Straight line shows theoretical dependence assumed [Eq. (8)].



## B. Corrections

The values obtained for the cross section when plotted as a function of the local zenith angle  $\chi$  (Fig. 3) exhibit the twin effects of terrestrial atmospheric extinction and the systematic variation of antenna gain with elevation noted earlier.<sup>10,11</sup> The zenith angle dependence appears to be slightly different from that found previously, due, probably, to increased atmospheric extinction encountered in summer when the humidity is high.<sup>12</sup> Accordingly, the two-way zenithal absorption was taken as 0.114 db and an antenna sag correction was used based on measurements reported by Allen.<sup>10</sup> Figure 3 shows the fit of uncorrected experimental data to the combined extinction and sag law.

The one-way atmospheric extinction law used was given by

$$L_1 = \exp(-0.0131 \sec \chi) \quad . \quad (6)$$

The antenna sag correction could be fitted to the same form of expression and for unity correction at 50° zenith angle

$$L_2 = 1.0443 \exp(-0.0279 \sec \chi) \quad . \quad (7)$$

The composite two-way correction formula used in the radar cross section computations was  $(L_E)^2 = (L_1 L_2)^2$  or

$$L_E^2(\chi) = 1.09 \exp(-0.082 \sec \chi) \quad . \quad (8)$$

By this means, the computations of radar cross section were corrected for the effects of normal atmospheric attenuation and antenna gain variations with elevation angle.

On days during which the weather is adverse, rain and heavy clouds can cause excess atmospheric attenuation of considerable variability. Fortunately, during the CW Hayford series of experiments, a correction for weather attenuation was required for only 2 days, 3 and 10 August. The system temperature measured after each run was used to estimate the excess temperature caused by the weather conditions. This excess was taken as the difference between the measured temperature and the normal value of 75°K experienced with the receiving system during this period. The excess temperature was assumed to be due to attenuation in a 290°K atmosphere of a source outside the atmosphere having a temperature of 20°K (see Ref. 11). The resulting attenuation factor  $L_v$  was used in the radar cross section computations on 3 and 10 August to make a first order correction for weather. The maximum correction was only 5 percent of the derived cross section, so that a large error should not arise.

## C. Accuracy

During the series of Hayford CW measurements, the signal-to-noise ratio was extremely high for a planetary radar type of measurement. The primary sources of error in estimating the radar cross section of Venus are, therefore, principally the uncertainties in the radar system parameters, especially those that varied during the course of a run, such as the transmitted power, system temperature, or the antenna pointing. Table IV lists the uncertainties that have been assigned to each of the radar parameters. Two values are given — the absolute uncertainty of each parameter and a relative value indicating the accuracy to which the parameter can be expected to change from run to run without detection. Because of the fact that the radar

TABLE IV ESTIMATED ACCURACY OF RADAR PARAMETERS		
Parameter	Uncertainty (percent)	
	Relative	Absolute
Antenna gain $G_t$	0	$\pm 20$
Antenna aperture $A_r$	0	$\pm 20$
Transmitter power $P_t$	$\pm 10$	$\pm 20$
System temperature $T_s$	$\pm 10$	$\pm 20$
System losses $L_s$	0	0
Extinction correction $L_E$	$\pm 2$	$\pm 5$

system could not be operated against targets at short ranges, no direct radar system sensitivity measurements on calibration spheres or similar targets were possible.

Determination of the antenna performance was based upon radio astronomical observations.<sup>13</sup> Strictly speaking, these measure the antenna performance with the receiver waveguide configuration slightly different from that used in the CW radar mode. The transmitter uses a waveguide system that is not common to the receiving path except close to the antenna horn feed, and an extra transmit line loss of 0.5 db was included in the computations of radar cross section to account for this difference. The value of the antenna gain (66.1 db) used for the computation of  $\sigma$  is believed to have an uncertainty of  $\pm 20$  percent at most. Any inaccuracy in the pointing due, for example, to antenna servo perturbations would serve to lower the effective antenna gain. However, the accuracy of the pointing was checked radiometrically so that considerable confidence could be placed in the pointing ephemeris, and the servo tracking.

The transmitter output power was monitored by calibrated power meters. The accuracy of this monitoring system was checked with calorimetric heat measurements and knowledge of DC transmitter input power and klystron efficiency. The actual measurement accuracy available with this monitoring system is better than indicated in the table. However, because the value logged by the operator was not the mean value for the entire run, we are forced to assign a larger uncertainty. Early in the day, for example, the power would build up during the transmit period. There were also some runs during which there were momentary shutdowns of RF power, typically for 10 seconds, which were not always logged. Both of these effects would result in an overestimate of the average power in the logged values. The radar operating procedure has since been modified to identify specifically those runs free of this type of problem, and hence valid for cross section measurement. Runs during the Hayford experiment where this type of problem was identified were eliminated from the computations.

The measurement of system temperature was crucial in the calibration of the output spectra and hence in the measurement of radar cross section. The system temperature was measured by injecting a known level of noise into the receiver from a gas discharge source. The injection level of the noise source had been previously calibrated by substitution of hot and cold loads to

within an estimated accuracy of  $\pm 20$  percent. The increase in noise level in the receiver was measured with a precision attenuator in a "Y factor measurement" and the corresponding system temperature logged at the end of each run. This is a spot measurement and can be a source of inaccuracy if the system temperature changes during the receive period (as would be the case during rain). The temperature measurement would also be inaccurate in the presence of interference as it was performed in a 10-MHz bandwidth while the actual data processing was limited to a band of the order of 1 kHz. Also, since the measurement was done manually during the press of operations, there is the possibility of human error. A relative uncertainty of  $\pm 10$  percent is assigned to this factor.

The limb-to-limb Doppler spread used in the calculation of the cross section [i.e., the value of  $B$  that should be employed in Eq. (3)] was obtained from previously prepared ephemerides. An error in the limb-to-limb Doppler value would have only a second order effect on the cross section measurement because of the small amount of power returned from the limbs of the planet. The remaining parameters in the radar equation such as bandwidth and radar round trip delay are known to much greater accuracy than is significant in the cross section computations.

TABLE V  
SIGNAL-TO-NOISE COMPUTATIONS  
(Run 22804, 16 August 1967)

Round trip delay $t_R$	312.345 sec
Receive integration time	265 sec
System temperature $T_S$	84.1°K
Equivalent filter bandwidth	1 Hz
Theoretical rms noise	5.17°K
Measured 1 standard deviation	6.01°K
Peak spectral temperature	3276°K
Signal power sum	84,506°K
Limb-to-limb Doppler	145.2 Hz
Number of filters in sum $m$ [Eq. (3)]	$2 \times 145$
Theoretical 1 standard deviation sum	71.3°K

The effects of additive noise were considered and found to be insignificant except in the measurement of scattering law near the planetary limb. Estimates of the effects of noise are given in Table V for Run 22804 on 16 August. With a filter noise bandwidth of 1 Hz and an integration time of 265 seconds, the standard deviation value of the filter outputs should be 5.17°K for a system temperature of 84.1°K. The signal sum used to estimate total signal power was 84,500°K. The rms uncertainty of this sum due to additive gaussian noise was computed to be only 71.3°K. The self-noise of the Venus signal itself is a much greater source of error. If (for the purposes of error estimate) the spectrum is assumed to be a narrow band gaussian function with a peak value of 3000°K per Hz and an effective bandwidth of 28 Hz, then the rms uncertainty in the sum [Eq. (5)] would be about 1000°K. That is, the temperature (84,500°K) can

be compared with the statistical uncertainty of  $1000^\circ\text{K}$ , and an uncertainty due to additive noise of  $70^\circ\text{K}$ . Thus the accuracy of the measurements is primarily limited by the knowledge of system parameters (see Table IV) rather than by noise.

In summary, the absolute system calibration accuracy (and hence the accuracy of  $\sigma$ ) is believed to be about  $\pm 50$  percent (i.e.,  $\pm 2$  db) and the relative accuracy from run to run or day to day about  $\pm 20$  percent (i.e.,  $\pm 1$  db).

## D. Results

### 1. Average Value at Inferior Conjunction

The corrected cross section  $\sigma$  obtained in the Hayford experiment for each data block is presented in Table III. The mean value for the cross section is 1.74 percent of the projected area of the disk, which is in close agreement with the value obtained earlier.<sup>11</sup> The values are plotted as a function of date in Fig. 4. It can be seen that no significant changes in cross section were observed during this period. This is similar to the behavior observed near inferior conjunction in 1966.<sup>11,14</sup>

The 60- $\mu\text{sec}$  coded pulse experiments provide echoes of sufficient intensity to permit an estimate of the cross section to be attempted. Accordingly, the echo energy with respect to delay and frequency was summed in order to derive  $P_r$  [Eq. (1)]. Unfortunately, the uncertainty in the noise baseline makes this a somewhat inaccurate process. In addition, there remains the problem of foldover of the echo in delay which requires for its removal a large and uncertain correction. Accordingly, we have normalized these values to have the same mean value (1.74 percent) as obtained in the CW experiments and have included them, together with the results of Fig. 4, in Fig. 5. These additional points reinforce the suggestion that there is a slight dip in  $\sigma$  between days 220 and 230, but as the error estimates above indicate, this is equally likely to be instrumental in origin.

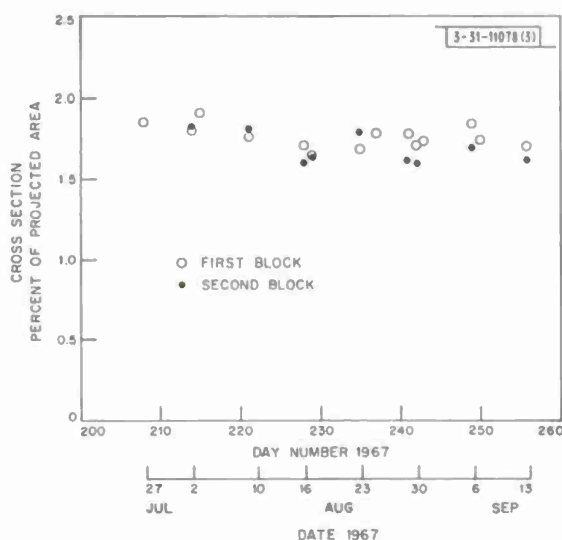


Fig. 4. Variation of radar cross section around inferior conjunction (30 August) as obtained from Hayford CW results.

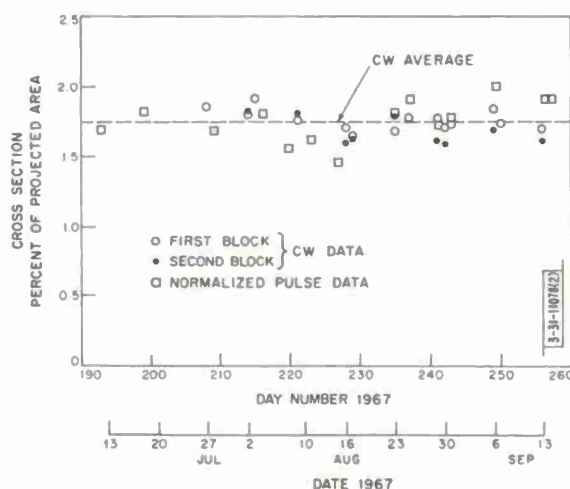


Fig. 5. Pulse measurements of radar cross section of Venus near inferior conjunction together with Hayford CW results (Fig. 3). Pulse measurements have been normalized to same mean value.



The average value of the cross section presented here supports the conclusion that the radar cross section of Venus at 3.8 cm is  $\sim 8$  db lower than observed at the next highest wavelength ( $\lambda = 12.5$  cm) at which measurements have been made.<sup>15</sup> As noted by earlier investigators<sup>16,14</sup> it seems extremely unlikely that this large difference can arise from the frequency dependence of the reflection coefficient of the surface. The most likely source of error in this estimate would be improper calibration of either of the two radar systems. As noted above for Haystack, the absolute calibration is believed to be accurate to  $\pm 50$  percent, and the day-to-day repeatability somewhat better than this. It is thought that the calibration of the JPL radar has been carried out to an accuracy of better than  $\pm 2$  db and thus the cross section difference is  $8 \pm 3$  db.

## 2. Average Value for 1967

The range of planetary longitudes spanned by the results presented in Fig. 5 is quite small ( $\sim 60^\circ$ ) due to the fact that the apparent angular velocity of the planet is least at inferior conjunction. Unfortunately it was not possible in this set of observations to examine the longitudes covered in 1966 at which the cross section was seen to increase. Some CW measurements were made in April 1967. These contained fewer runs than in the Hayford measurements and are probably less accurate. These observations yielded the cross section values summarized in Table VI. The average of these is 1.53 percent, i.e., somewhat less than the average value observed near the inferior conjunction (Table IV) but this may not be significant. The average for all the observations in 1966 is  $1.69 \pm 0.14$  percent where the uncertainty quoted is the rms deviation from the mean. The absolute uncertainty is, however, probably somewhat larger as noted above.

TABLE VI					
CW MEASUREMENTS OF RADAR CROSS SECTION					
Block No.	Date (1967)	Time (GMT)		No. of Runs	Percent Cross Section
		First	Last		
100-1	10 April	2059	2142	2	1.33
102-1	12 April	1746	1912	3	1.45
103-1	13 April	1815	—	1	1.34
104-1	14 April	1913	2119	4	1.76
111-1	21 April	1933	2055	3	1.76
116-1	26 April	2055	2215	3	1.50
207-1	26 July	1825	1910	4	1.54
					mean = 1.53%

## 3. Cross Section vs Longitude

Table VII summarizes all the 3.8-cm CW cross section measurements obtained to date at Haystack together with the coordinates of the subradar point at noon on these days. A single value is given for each day's observation, which in the case of the results presented in Table IV is simply a mean of any two values listed. The earlier values are those presented in Ref. 11. These values of cross section are plotted as a function of longitude in Fig. 6.

TABLE VII  
SUMMARY OF 3.8-cm CW RADAR CROSS SECTION MEASUREMENTS

Year	Date	Subradar Position at Noon <sup>1</sup>		Cross Section (percent $\pi r_o^2$ )
		Longitude (deg)	Latitude (deg)	
1966	18 Jan	316.69	-5.61	1.74
	1 Feb	329.28	-8.07	1.32
	9 Feb	337.72	-8.27	1.61
	21 Mar	52.48	-3.45	1.77
	30 Mar	73.72	-2.26	2.51
	15 Apr	113.11	-0.41	3.50
	5 May	164.09	+1.28	1.60
	17 May	195.24	+1.94	2.75
	15 June	271.51	+2.43	2.10
	27 June	303.36	+2.26	1.75
1967	10 Apr	2.36	-0.59	1.33
	12 Apr	7.69	-0.68	1.45
	13 Apr	10.36	-0.73	1.34
	14 Apr	13.02	-0.77	1.76
	21 Apr	31.66	-1.08	1.76
	26 Apr	44.88	-1.29	1.50
	26 Jul	266.69	+2.53	1.54
	27 Jul	268.60	+2.70	1.86
	2 Aug	279.47	+3.85	1.81
	3 Aug	281.17	+4.06	1.92
	10 Aug	292.08	+5.53	1.79
	16 Aug	299.93	+6.79	1.66
	17 Aug	301.10	+6.99	1.65
	23 Aug	307.39	+8.03	1.73
	25 Aug	309.26	+8.30	1.79
	29 Aug	312.78	+8.67	1.70
	30 Aug	313.64	+8.74	1.66
	31 Aug	314.50	+8.78	1.74
	6 Sept	319.87	+8.72	1.77
	7 Sept	320.84	+8.66	1.74
	13 Sept	327.29	+8.04	1.67

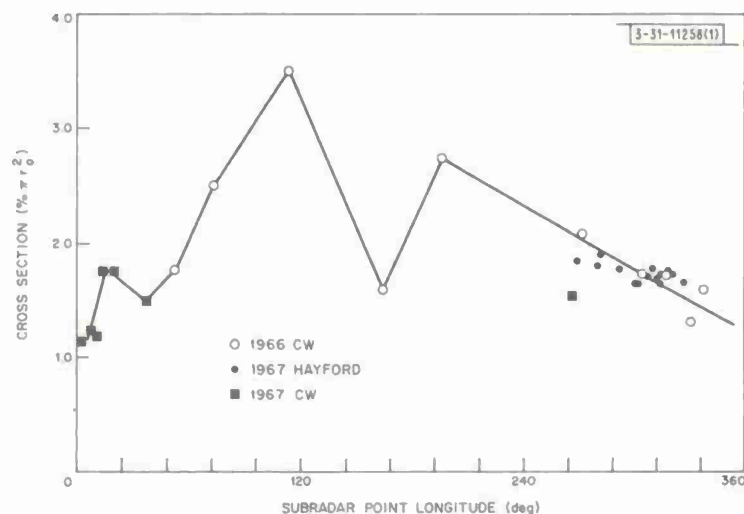


Fig. 6. Cross section of Venus vs subradar longitude based on all 3.8-cm observations of Venus made at Haystack to date (Table VII).

The longitude system employed here is identical to that of Ref. 1, namely, the prime meridian is taken to be the one proposed by Carpenter,<sup>15</sup> i.e., that meridian passing  $40^\circ$  to the west of the central meridian at 0.0 h U.T. on 20 June 1964. This system was chosen to place the prime meridian through an isolated anomalously bright scattering region (F in Carpenter's notation). This region no longer lies precisely on the prime meridian when specified in the above manner, since Carpenter adopted a rotation period of  $-250$  days while more recent results place it near  $-243.2$  days.<sup>17</sup> In Ref. 11 a coordinate system employed by I. I. Shapiro and co-workers was employed in which the prime meridian was defined as the central meridian at 0.0 h U.T. on 1 January 1961. Values of longitude in this system can be recovered by adding  $238.343^\circ$  to the values employed here.

It may be noted that though the system used here has the same prime meridian employed by Carpenter,<sup>15</sup> coordinates quoted in Ref. 15 will differ from those employed here because of the differences, as shown below, in the assumed rotation rate and the location of the pole position.

	Present System <sup>1</sup> and Ref. 11	Carpenter <sup>15</sup>
Pole Position}	$\delta = 66^\circ$	$\delta = 68^\circ$
	$\alpha = 270^\circ$	$\alpha = 255^\circ$
Rotation	$-243.2$ days	$-250$ days

Since the latitude of the subradar point does not wander far from the equator it should be possible in time to build up a complete plot of cross section vs longitude. It seems from Fig. 6 that where they overlap, the 1966 and 1967 values agree fairly well. This lends support to the view that the increases observed between longitudes of  $50^\circ$  and  $250^\circ$  are real. However, a large effort is needed to obtain coverage at other longitudes.

## V. THE ANGULAR SCATTERING LAW

### A. Mean Power Spectrum

The echo frequency power spectra derived in the manner outlined above have been averaged in the following way. First, because the overall limb-to-limb Doppler broadening  $2f_{\max}$  varies

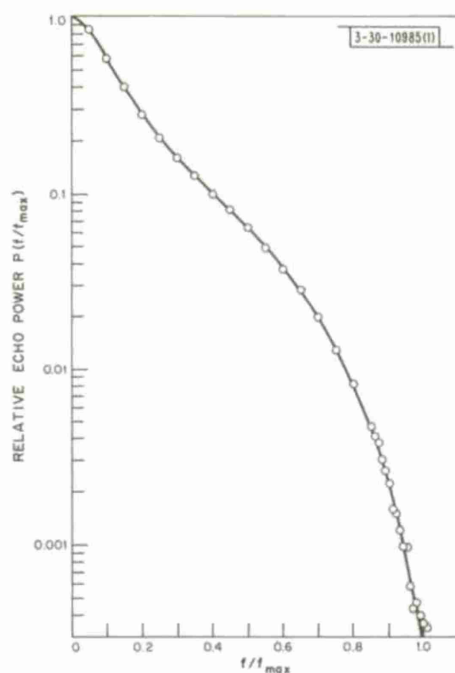


Fig. 7. Normalized mean frequency power spectrum  $\bar{P}(f/f_{\max})$  of Venus echoes observed in Hayford CW experiment.

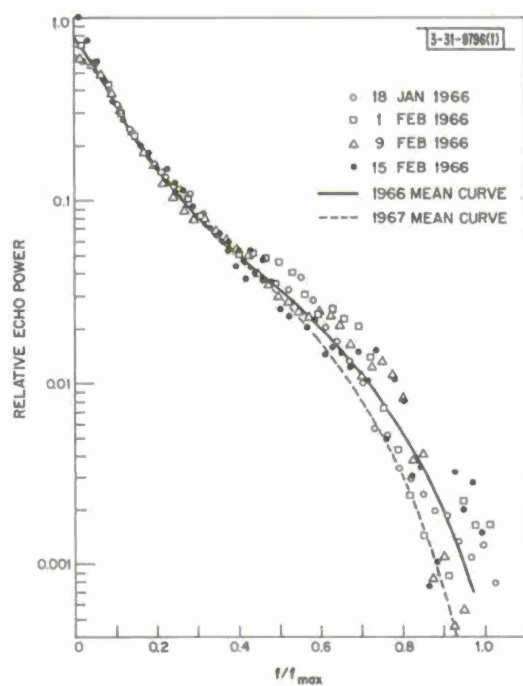


Fig. 8. Comparison of 1967 results shown in Fig. 7 with points obtained on 4 days in 1966.

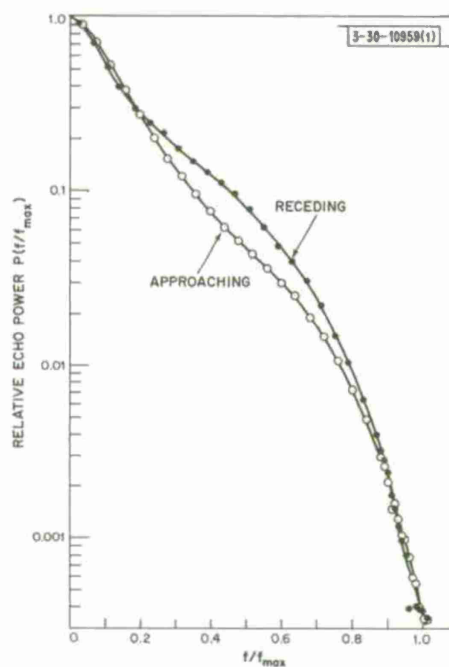


Fig. 9. Comparison of mean frequency power spectra  $\bar{P}(f/f_{\max})$  observed for Venus echoes in Hayford CW experiment for approaching and receding halves of disk.

as a function of time, it is necessary to replot all the power spectra against a normalized frequency scale  $f/f_{\max}$ . This has been accomplished by computing  $f_{\max}$  for each observing block using the most recent estimate of the rotation period of Venus<sup>17</sup> and dividing the echo power into 200 intervals spanning the range  $-f_{\max}$  to  $+f_{\max}$  by straight linear interpolation. An estimate of the Doppler shift of the Venus echo, based upon an examination of many spectra, suggested that the signals recorded during this period were offset by  $-1$  Hz with respect to the  $+100$ -Hz expected center frequency. Accordingly, a correction for this frequency bias was applied before the spectra were normalized to a common frequency scale. Later analysis indicated that this correction was not necessary, but since the effect was small the data have not been reprocessed.

Next a mean was taken of the cross section vs frequency  $\sigma(f/f_{\max})$  curves. In this way all runs were weighted equally, i.e., variations in power due to changes in  $P_t$ ,  $G$ ,  $A$ , or  $R$  [Eq. (1)] with date were removed. This mean spectrum  $\bar{\sigma}(f/f_{\max})$  was then normalized to be unity at  $f = 0$ . Figure 7 shows the mean power spectrum obtained when the data from both the approaching and receding hemispheres are averaged. The small scatter of the points near  $f/f_{\max} \rightarrow 1.0$  is indicative of the high experimental accuracy achieved in the measurements. In Fig. 8 we compare this curve with four spectra obtained in 1966, and the mean curve that was drawn through them.<sup>14</sup> The agreement for  $0 < f/f_{\max} < 0.5$  is considered good, but thereafter the new curve departs systematically beneath the old.

Figure 9 compares the signal spectra obtained for the approaching and receding halves of the disk. They are clearly different — an effect evident earlier.<sup>14</sup> This difference stems from the presence of regions on the surface that on the scale of the wavelength are rougher than their environs and which therefore appear bright in a reflectivity plot (see Sec. VI). The locations of some of these features have been determined by Goldstein<sup>18,19</sup> and Carpenter<sup>15</sup> and are discussed in Sec. VI. During the present observing period, anomalously reflecting areas could be expected principally on the receding side where B, C and D (in Carpenter's notation) would lie. The reflectivity of these features with respect to the surrounding terrain can be judged approximately from the echo peaks they produce in the spectra. These are found to be significantly larger at  $3.8$  cm than at  $12.5$  cm, due either to their increased effective roughness at the shorter wavelength, their elevation above the surrounding terrain (and hence the reduced absorption to their tops) or a combination of these effects.<sup>11</sup> The apparent rotation of the planet has smeared the contributions from these regions so that in Fig. 9 they no longer give rise to discrete features. In what follows the spectrum obtained for the approaching side is employed to derive the angular power spectrum, since this is contaminated to lesser degree by reflections from anomalously scattering regions. Table VIII lists values of the relative echo power observed here. Also listed in this table are values (the average of both sides) obtained from the mean spectrum published by Muhleman<sup>20</sup> based upon observations at  $12.5$  cm. At this wavelength the anomalously scattering regions appear less bright so that there is no pronounced asymmetry in the two halves of the spectrum.

## B. Angular Power Spectrum $P(\varphi)$

If it is assumed that the scattering properties of the planetary disk are uniform, the brightness distribution will exhibit radial symmetry about the subradar point. The echo power spectrum  $\bar{P}(f)$  can then be employed to yield the echo power  $\bar{P}(\varphi)$  reflected per unit surface area per unit solid angle as a function of the angle of incidence (and reflection)  $\varphi$ .<sup>21</sup> Measurements and

TABLE VIII		
RELATIVE ECHO POWER VS FREQUENCY FOR VENUS		
$f/f_{\max}$	Relative Power 3.8 cm (approaching)	Relative Power 12.5 cm
0	1.0000	1.000
0.05	0.8445	0.660
0.10	0.6119	0.410
0.15	0.4094	0.270
0.20	0.2746	0.192
0.25	0.1872	0.146
0.30	0.1358	0.112
0.35	0.1007	0.0895
0.40	0.0768	0.0720
0.45	0.0591	0.0586
0.50	0.0475	0.0480
0.55	0.0373	0.0407
0.60	0.0296	0.0342
0.65	0.0232	0.0288
0.70	0.0168	0.0242
0.75	0.0114	0.0197
0.80	0.0073	0.0157
0.85	0.0043	0.0123
0.90	0.0021	0.00944
0.95	0.0010	0.00660
1.00	0.0000	0.00190

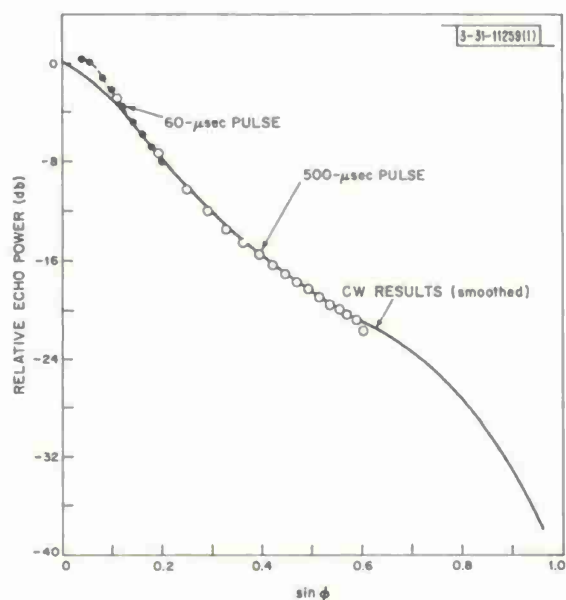


Fig. 10. Mean angular power spectrum  $\bar{P}(\phi)$  derived from data shown in Fig. 9 for approaching hemisphere, together with points obtained from variation of echo power vs delay observed with 60- and 500-μsec pulses.



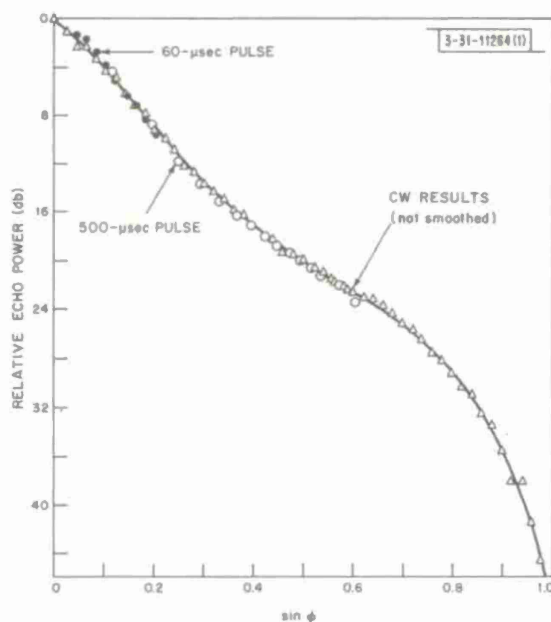
transformations of this type for Venus were first performed by Goldstein<sup>22</sup> and Carpenter<sup>23</sup> at 12.5-cm wavelength. Here the transformation has been carried out using the Bessel transform routine developed by T. Hagfors (private communication) that was described previously.<sup>14,21</sup> The result of transforming the spectrum of Fig. 9 for the approaching side (Table VIII) is shown in Fig. 10.

In order to check the accuracy of the results plotted in Fig. 10, we have employed the results obtained for the average echo power vs delay  $\bar{P}(t)$  in the Hayford Coded and Fourth Test ranging experiments (Sec. III-C and -D, respectively). Here the transformation of echo power vs  $\varphi$  is straightforward since

$$\cos \varphi = 1 - ct/2r_0 \quad (9)$$

where  $t$  is the incremental delay (i.e., measured from the leading edge of the echo),  $c$  is the velocity of light and  $r_0$  the planetary radius. These results are also shown in Fig. 10 after translating the points vertically to achieve a "best fit" to the CW curve. The pulse data were useful only over the range  $3^\circ < \varphi < 35^\circ$ . Angles smaller than  $3^\circ$  cannot be explored because of the finite length of the pulse and the curvature of the surface. For  $\varphi > 35^\circ$  the errors become large owing to the inaccuracy with which the baseline could be established (see Sec. III). In the range  $9^\circ < \varphi < 35^\circ$ , the agreement between the two results shown in Fig. 10 is considered good and supports the procedure adopted.

Fig. 11. Mean angular power spectrum  $\bar{P}(\varphi)$  derived from data shown in Fig. 9 for approaching hemisphere when no weighting is applied to autocorrelation function used in Bessel transformation routine.<sup>14</sup>



For  $\varphi < 9^\circ$  the pulse data departs systematically above the CW result. It is possible that in part this has been caused by the linear weighting applied to the autocorrelation function derived from the mean power spectrum before the Bessel transformation is applied.<sup>14</sup> This weighting serves to remove fine structure from  $P(\varphi)$  but does tend to round the peak.<sup>14</sup> Accordingly, the transformation was repeated with no weighting and Fig. 11 shows the results obtained (triangles). A greater scatter of the points owing to the presence of unsuppressed high frequency components is evident in this figure but is not as pronounced as that encountered when treating the 1966 results.<sup>14</sup> Also evident from Fig. 11 is a closer agreement between the pulse and the CW data

TABLE IX  
RELATIVE ECHO POWER VS ANGLE OF INCIDENCE FOR VENUS

Sin $\Phi$	$\Phi$	Delay (msec)	Relative Power at 3.8 cm (db)	
			(Smoothed)	(Unsmoothed)
0.00000	0	0.000	0.000	0
0.02000	1° 9'	0.008	-0.340	-0.52
0.04000	2° 18'	0.032	-0.990	-1.27
0.06000	3° 26'	0.072	-1.552	-2.10
0.08000	4° 35'	0.129	-2.247	-2.96
0.10000	5° 44'	0.202	-3.087	-3.83
0.12000	6° 54'	0.291	-3.897	-4.79
0.14000	8° 3'	0.397	-4.829	-5.74
0.16000	9° 12'	0.520	-5.818	-6.79
0.18000	10° 22'	0.659	-6.720	-7.78
0.20000	11° 32'	0.816	-7.671	-8.76
0.22000	12° 43'	0.989	-8.609	-9.70
0.24000	13° 53'	1.180	-9.520	-10.61
0.26000	15° 4'	1.389	-10.468	-11.56
0.28000	16° 16'	1.616	-11.288	-12.68
0.30000	17° 27'	1.860	-12.044	-13.13
0.32000	18° 40'	2.124	-12.811	-13.90
0.34000	19° 53'	2.406	-13.524	-14.61
0.36000	21° 6'	2.708	-14.243	-15.33
0.38000	22° 22'	3.030	-14.915	-16.01
0.40000	23° 35'	3.372	-15.542	-16.63
0.42000	24° 50'	3.736	-16.194	-17.28
0.44000	26° 6'	4.120	-16.835	-17.93
0.46000	27° 23'	4.528	-17.471	-18.56
0.48000	28° 4'	4.958	-18.009	-19.10
0.50000	30° 0'	5.412	-18.463	-19.55
0.52000	31° 20'	5.891	-18.968	-20.06
0.54000	32° 41'	6.396	-19.504	-20.59
0.56000	34° 3'	6.928	-20.040	-21.13
0.58000	35° 27'	7.489	-20.541	-21.63
0.60000	36° 52'	8.080	-21.008	-22.10
0.62000	38° 19'	8.702	-21.480	-22.57
0.64000	39° 48'	9.357	-21.907	-23.00
0.66000	41° 18'	10.048	-22.354	-23.44
0.68000	42° 51'	10.778	-22.906	-24.00
0.70000	44° 26'	11.548	-23.515	-24.61
0.72000	46° 3'	12.363	-24.172	-25.26
0.74000	47° 45'	13.226	-24.898	-25.99
0.76000	49° 28'	14.143	-25.676	-26.77
0.78000	51° 16'	15.118	-26.488	-27.58
0.80000	53° 8'	16.160	-27.354	-28.44
0.82000	55° 5'	17.276	-28.283	-29.37
0.84000	57° 8'	18.479	-29.259	-30.35
0.86000	59° 19'	19.784	-30.342	-31.43
0.88000	61° 39'	21.211	-31.599	-32.69
0.90000	64° 9'	22.790	-33.078	-34.17
0.92000	66° 55'	24.566	-34.648	-35.74
0.94000	70° 3'	26.616	-36.106	-37.20
0.96000	73° 44'	29.088	-37.940	-39.03
0.98000	78° 31'	32.360	-41.180	-42.27
1.00000	90°	40.399	-92.999	-94.09



(cf. Fig. 10). By using the curve obtained without smoothing (Fig. 11) in the range  $0 < \sin \varphi \leq 0.2$  together with the smoothed data (Fig. 10) for  $0.2 \leq \sin \varphi < 1.0$  we have obtained what we believe is the best curve available for  $P(\varphi)$ . This is shown as the full curve of Fig. 11 and values taken from this curve are listed in Table IX.

### C. Effects of Refraction in the Atmosphere of Venus

The method of obtaining the angular scattering law  $\bar{P}(\varphi)$  employed here involves the assumption of the rectilinear propagation of waves reflected by a solid body in rotation. The presence of the atmosphere of Venus can influence the results in a number of ways. The atmosphere will refract waves toward the local normal as shown in Fig. 12, thereby reducing the angle  $\varphi$  at which they encounter the surface.<sup>24</sup> In addition, since the refractive index of the atmosphere differs from unity and because the path is now curved, the total time delay will also be changed. In this section we discuss these effects in order to estimate the extent to which they have modified the function for  $\bar{P}(\varphi)$  obtained.

The effects of refraction in deep planetary atmospheres have been discussed by Phinney and Anderson<sup>25</sup> among others. It is useful to define an impact parameter  $p = nr \sin i$  (Fig. 13) which is constant along any ray, by Snell's law. Here  $n$  is the refractive index at any point along the path and varies from  $n = 1$  at a point  $r = r_\infty$  sufficiently distant from the planet to  $n = n_s$  at the

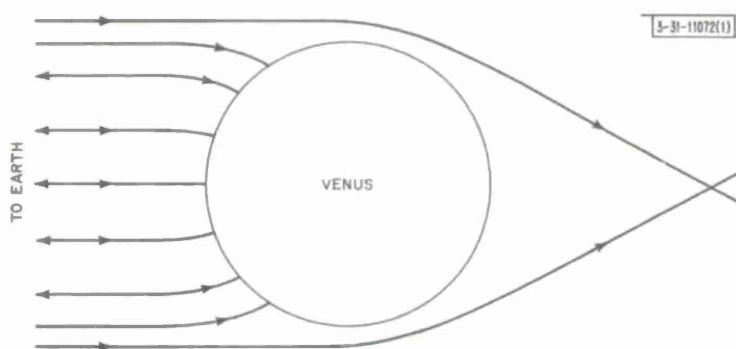


Fig. 12. Wave refraction in atmosphere of Venus.

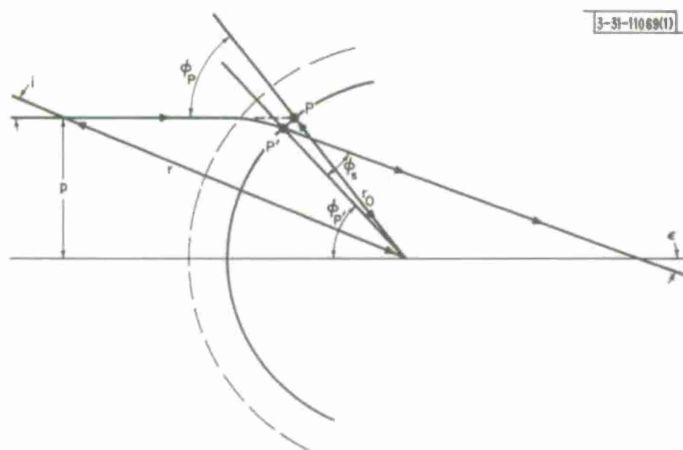


Fig. 13. Bending of single ray in atmosphere of Venus.

surface ( $r = r_0$ ). As may be seen in Fig. 13,  $p$  is the radial distance from the center of the disk to the point  $P$  at which the ray would arrive in the absence of any atmosphere. It follows that

$$p = r_0 \sin \varphi_P \quad (10)$$

When refraction takes place, the ray arrives instead at  $P'$  having been bent through the angle  $\epsilon$ . At the surface

$$p = r_0 n_s \sin \varphi_s \quad (11)$$

where  $\varphi_s$  is the local zenith distance to the ray. From Eqs. (10) and (11), it follows that

$$\sin \varphi_s = \sin \varphi_P / n_s \quad (12)$$

The optical path length encountered by the ray while traversing the atmosphere from a plane of constant phase in front of the planet down to the planetary surface is

$$R = \int_{r=r_0}^{\sqrt{r_\infty^2 + p^2}} \frac{ndr}{\cos i} \quad (13a)$$

$$= \int_{r=r_0}^{\sqrt{r_\infty^2 + p^2}} n [1 - (p/nr)^2]^{-1/2} dr \quad (13b)$$

In the case of pulse observations, these effects will serve to change the relationship between  $\varphi$  and delay  $t$  [Eq. (9)]. In Fig. 13, for example, signals returned from a point  $P'$  would be assigned an angle of incidence  $\varphi_{P'}$  (neglecting the additional delay due to path curvature). Actually, the local angle of incidence will be  $\varphi_s$  and the error

$$\varphi_{P'} - \varphi_s = \epsilon \quad (14)$$

The additional delay encountered in the atmosphere due to bending and the increased refractive index will depend upon the impact parameter  $p$  and will serve to raise the incremental delay  $t$  for rays traversing the atmosphere obliquely. This will increase the value of  $\varphi_{P'}$ , deduced via Eq. (9), and hence the net error in the assumed angle of incidence will be somewhat larger than  $\epsilon$ .

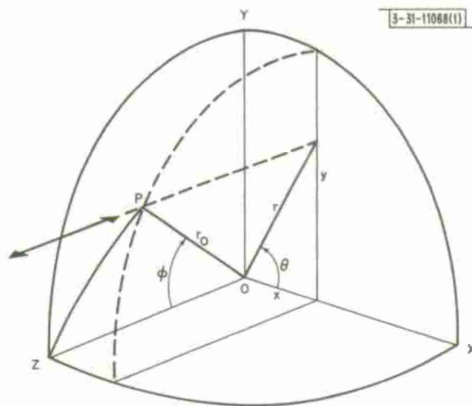


Fig. 14. Geometry for calculating Doppler shift of reflected ray.

Fig. 13 is redrawn in Fig. 14 where one quarter of the hemisphere visible from earth is shown. Here,  $OZ$  is the direction of the earth, and the plane  $OXY$  contains the apparent spin axis. When

projected upon the plane OXY, the point P lies at (xy). In the absence of any atmosphere, the Doppler shift encountered for the ray reflected at P will be

$$\Delta f_P = \frac{2}{\lambda} \left( \frac{dR}{dt} \right) \quad (15a)$$

$$= \frac{+2\omega r_0 \cos \Theta \sin \varphi}{\lambda} \quad (15b)$$

where  $\omega$  is the apparent angular velocity and it is assumed that P lies on the approaching half of the disk. The locus of points on the projected disk having the same Doppler shift is set by

$$r_0 \cos \Theta \sin \varphi = \text{const} \quad \text{i.e.,} \quad x = \text{const}.$$

Thus, in the absence of an atmosphere, the disk may be imagined as ruled by lines parallel to the projected spin axis, each of which is a locus of constant Doppler shift [Fig. 15(a)]. When atmospheric refraction is present, the ray approaches the surface as shown in Fig. 13 and arrives at the point P' lying at (x'y') on the projected disk. The Doppler shift is again given by Eq. (15a) and may be considered the sum of two terms, viz., (1) a term akin to Eq. (15b) representing the velocity of approach of the reflection point, and (2) a term which depends upon the rate of change of additional phase path length due to the presence of the atmosphere. Since the additional phase path length increases approximately as  $\sec \varphi$ , this second term is likely to dominate as  $\varphi \rightarrow 90^\circ$ . The first term is

$$\text{Shift due to motion of reflection point} = \frac{2\omega r_0 \cos \Theta \sin \varphi_s}{\lambda} \quad (16)$$

Since  $\varphi_s$  and  $\epsilon$  are related in Eq. (14), this can be written as

$$= \frac{2\omega r_0 \cos \Theta \sin \varphi_{P'} \cos \epsilon}{\lambda} \quad (17)$$

for small  $\epsilon$ .

Evidently, if the bending of the rays were the only effect, the condition of constant Doppler shift would be

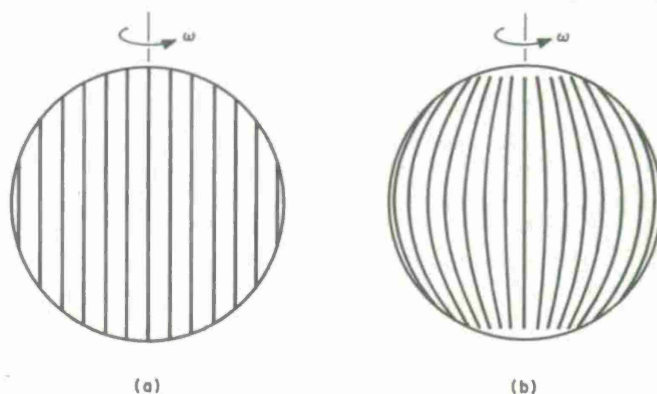
$$\cos \Theta \sin \varphi_{P'} \cos \epsilon = \text{const}.$$

$$\therefore x' \cos \epsilon = \text{const}$$

and the contours of constant Doppler shift would now be "bowed" as shown in Fig. 15(b). Under these circumstances, the Bessel transformation routine employed to convert  $\bar{P}(t)$  to  $\bar{P}(\varphi)$  must

3-31-11071(1)

Fig. 15. Schematic representation of contours of constant Doppler shift on disk of Venus (a) in absence of atmosphere refraction and (b) with severe refraction effects.



be invalid. However, for small frequency shifts, the echo power spectrum  $\bar{P}(f)$  is dominated by the behavior near the subradar point ( $\varphi$  small), and thus it seems likely that the curves shown in Figs. 11 and 12 are not seriously in error for  $\varphi$  less than some value  $\varphi_{\max}$ . As an order of magnitude estimate, we shall suppose that Venus has a  $\text{CO}_2$  atmosphere (refractivity of  $\text{CO}_2$  is  $\sim 1.5$  times that of air), with a surface pressure of 100 atmospheres. For small  $\varphi$  then,

$$\epsilon_{\text{Venus}} \approx 150 \epsilon_{\text{earth}} \quad (18)$$

For a zenith distance on earth  $\varphi = 60^\circ$ ,  $\epsilon = 1.6$  arc min, and thus on Venus would be of the order of  $4^\circ$ . Thus, if the change in the zenith distance to the ray were the only effect, it would seem that the curve for  $\bar{P}(\varphi)$  would be valid to  $\varphi \approx 60^\circ$ . In point of fact, the rate of change of additional path length (second term) serves to oppose the reduction in the Doppler shift brought about by the decrease in the zenith distance. This is because the phase shift is largest for those paths that traverse the atmosphere obliquely. In order to make accurate estimates of the combined effects, it is necessary to adopt a model for the properties of the atmosphere and solve Eq. (13) by numerical means. Such calculations have been carried out at M.I.T. (I. I. Shapiro, private communication) and confirm that the curve for  $\bar{P}(\varphi)$  is valid over  $0^\circ < \varphi \leq 60^\circ$ .

#### D. Absorption by the Atmosphere of Venus

The low value of the cross section reported here and found earlier<sup>16,14</sup> suggests that the signals reflected at 3.8 cm have been attenuated in the atmosphere of Venus. This will cause the intensity for any ray to be reduced by a factor  $\exp(-2\tau)$  where  $\tau$  is the "optical depth" defined in

$$\tau = \int_0^\infty K \sec \varphi \, dh \quad (19)$$

where  $K$  is the absorption coefficient per vertical height element  $dh$  and  $\varphi$  the local zenith angle. Since most of the energy is reflected from the center of the disk, we may write to a first approximation

$$\sigma = \sigma_0 \exp(-2\tau_0) \quad (20)$$

where  $\sigma_0$  is the intrinsic cross section (observable in the absence of an atmosphere) and  $\tau_0 = \int_0^\infty K dh$ . In the absence of refraction, the observed scattering law  $\bar{P}(\varphi)$  will be modified from the intrinsic law  $\bar{P}_0(\varphi)$  by absorption as in

$$\bar{P}(\varphi) = \bar{P}_0(\varphi) \exp(-2\tau \sec \varphi) \quad (21)$$

If  $\bar{P}_0(\varphi)$  were known from theory or some other way, the optical depth  $\tau$  could be determined from the secant dependence in Eq. (21). Previously<sup>14</sup> we attempted to circumvent the difficulty that  $\bar{P}_0(\varphi)$  is unknown by comparing curves of  $\bar{P}(\varphi)$  obtained at two frequencies. Thus the mean power spectrum results for 12.5 cm (Table VIII) published by Muhleman<sup>20</sup> were transformed to obtain  $\bar{P}(\varphi)$  by the same method as for the 3.8 cm results. Figure 16 compares the two curves. These (smoothed) values for  $\bar{P}(\varphi)$  at the two frequencies are also listed in Table X.

If the scattering properties of the surface of Venus at 3.8 and 12.5 cm were identical and the atmosphere introduced only absorption, we would expect the scattering laws  $\bar{P}(\varphi)$  observed



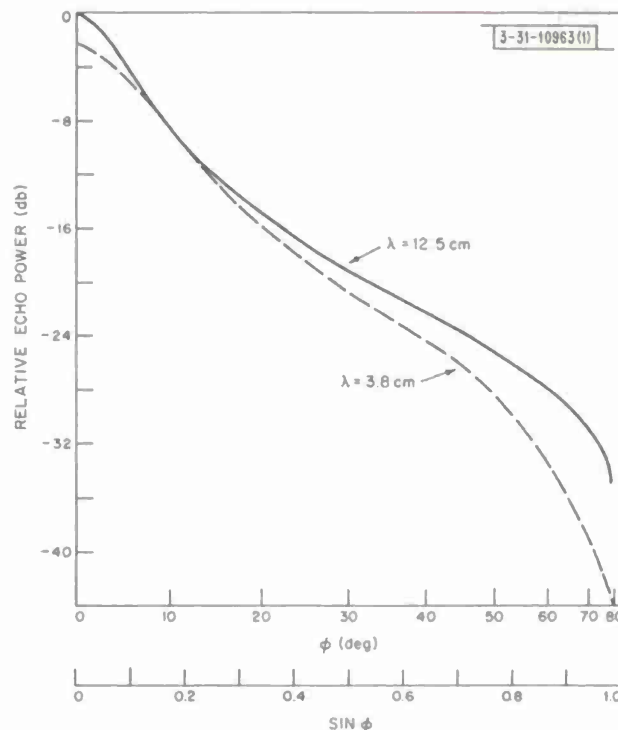


Fig. 16. Comparison of angular scattering laws  $\bar{P}(\phi)$  derived from the mean frequency power spectra  $\bar{P}(f/f_{\max})$  observed at 3.8 cm and 12.5 cm.

at the two wavelengths to be related in<sup>14</sup>

$$10 [\log_{10} \bar{P}(\phi)_{12.5} - \log_{10} \bar{P}(\phi)_{3.8}] = 2A \sec \phi \quad (22)$$

where  $A$  is the difference in the one-way zenithal absorption (db) in the Venus atmosphere at the two frequencies. When the effects of refraction are considered (above) this equation may be expected to break down. However, since the ray paths are the same at both frequencies, the difference in the two curves (Fig. 16) should be relatively insensitive to refraction effects at least up to  $\phi < \phi_{\max}$ .

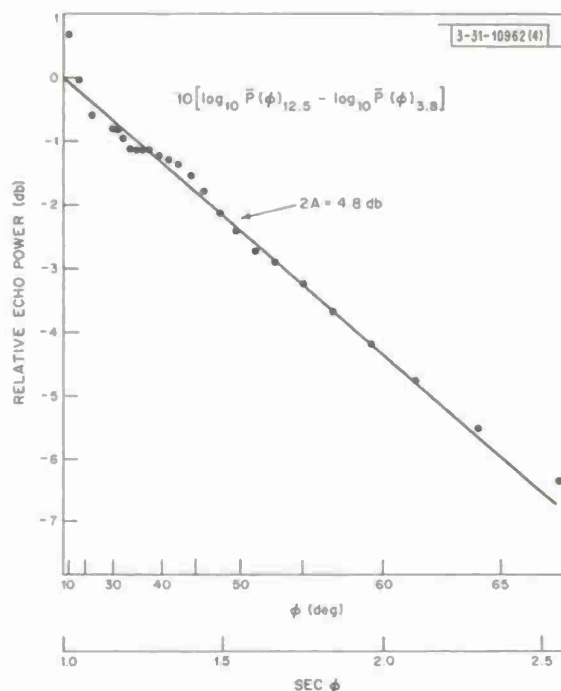
Since the effect of the smoothing applied in the Bessel transformation is unimportant for  $\sin \phi > 0.1$  and further because both spectra have been treated equally, no attempt has been made to recover the behavior near  $\phi \rightarrow 0^\circ$ . The difference shown in Fig. 16 is therefore not due to any smoothing but is a direct consequence of the more rounded peak of the 3.8 cm spectrum (Table VIII). This may represent a genuine difference in the intrinsic scattering behavior  $\bar{P}_o(\phi)$  at the two wavelengths (see Sec. V-E), but also probably results from the variation of  $\bar{P}(\phi)$  with the nature of the surface at the subradar point. As observed in 1966<sup>14</sup> (see Fig. 8) the behavior near  $\bar{P}(f) = 0$  does change with time. Thus the two curves have been adjusted to agree near  $\sin \phi = 0.2$ .

Figure 17 shows the difference between the two curves of relative echo power plotted in Fig. 16 as a function of  $\sec \phi$ . Over the range  $20^\circ < \phi < 60^\circ$ , the results fit a straight line quite well with the dependence  $2A = 4.8$  db. When the same comparison was attempted in 1966,<sup>14</sup> values in the range 5 to 7 db were obtained. The largest uncertainty was in the function  $\bar{P}(\phi)$  derived at 3.8 cm and confidence in the results was not high because the secant law, Eq. (22), was not obeyed as well as here.

TABLE X  
RELATIVE ECHO POWER VS ANGLE OF INCIDENCE FOR VENUS

Sin $\Phi$	$\Phi$	Delay (msec)	(Smoothed Data)	
			Relative Power for 3.8 cm (db)	Relative Power for 12.5 cm (db)
0.00000	0	0.000	0.000	0.000
0.02000	1° 9'	0.008	-0.340	-0.245
0.04000	2° 18'	0.032	-0.990	-0.958
0.06000	3° 26'	0.072	-1.552	-2.058
0.08000	4° 35'	0.129	-2.247	-3.388
0.10000	5° 44'	0.202	-3.087	-4.721
0.12000	6° 54'	0.291	-3.897	-5.884
0.14000	8° 3'	0.397	-4.829	-6.891
0.16000	9° 12'	0.520	-5.818	-7.879
0.18000	10° 22'	0.659	-6.720	-8.915
0.20000	11° 32'	0.816	-7.671	-9.915
0.22000	12° 43'	0.989	-8.609	-10.752
0.24000	13° 53'	1.180	-9.520	-11.432
0.26000	15° 4'	1.389	-10.468	-12.094
0.28000	16° 16'	1.616	-11.288	-12.829
0.30000	17° 27'	1.860	-12.044	-13.586
0.32000	18° 40'	2.124	-12.811	-14.247
0.34000	19° 53'	2.406	-13.524	-14.791
0.36000	21° 6'	2.708	-14.243	-15.318
0.38000	22° 22'	3.030	-14.915	-15.912
0.40000	23° 35'	3.372	-15.542	-16.533
0.42000	24° 50'	3.736	-16.194	-17.087
0.44000	26° 6'	4.120	-16.835	-17.561
0.46000	27° 23'	4.528	-17.471	-18.049
0.48000	28° 4'	4.958	-18.009	-18.617
0.50000	30° 0'	5.412	-18.463	-19.211
0.52000	31° 20'	5.891	-18.968	-19.712
0.54000	32° 41'	6.396	-19.504	-20.100
0.56000	34° 3'	6.928	-20.040	-20.479
0.58000	35° 27'	7.489	-20.541	-20.936
0.60000	36° 52'	8.080	-21.008	-21.438
0.62000	38° 19'	8.702	-21.480	-21.882
0.64000	39° 48'	9.357	-21.907	-22.245
0.66000	41° 18'	10.048	-22.354	-22.611
0.68000	42° 51'	10.778	-22.906	-23.051
0.70000	44° 26'	11.548	-23.515	-23.533
0.72000	46° 3'	12.363	-24.172	-23.975
0.74000	47° 45'	13.226	-24.898	-24.373
0.76000	49° 28'	14.143	-25.676	-24.820
0.78000	51° 16'	15.118	-26.488	-25.382
0.80000	53° 8'	16.160	-27.354	-26.007
0.82000	55° 5'	17.276	-28.283	-26.595
0.84000	57° 8'	18.479	-29.259	-27.129
0.86000	59° 19'	19.784	-30.342	-27.705
0.88000	61° 39'	21.211	-31.599	-28.388
0.90000	64° 9'	22.790	-33.078	-29.199
0.92000	66° 55'	24.566	-34.648	-29.838
0.94000	70° 3'	26.616	-36.106	-30.686
0.96000	73° 44'	29.088	-37.940	-32.038
0.98000	78° 31'	32.360	-41.180	-34.517
1.00000	90°	40.399	-92.999	-77.691

Fig. 17. Difference between curves of relative echo power plotted in Fig. 16 as a function of  $\sec \phi$ .



### E. Theoretical Behavior

Hagfors<sup>26</sup> (among many others) has discussed the scattering behavior of planetary surfaces at radio wavelengths. For many surfaces in which the auto-correlation function describing the horizontal variation of surface height is exponential, the power scattered per unit mean surface area per unit solid angle as a function of the angle of incidence  $\phi$  on the mean surface is of the form

$$P(\phi) \propto [\cos^4 \phi + C \sin^2 \phi]^{-3/2} \quad (23)$$

where  $C = (d'\lambda/4\pi h_o^2)^2$  is a constant in which  $d'$  defines the horizontal correlation scale,  $\lambda$  is the wavelength and  $h_o^2$  is the mean square height deviation of the surface.

The scattering of the moon and Venus can be characterized by two components. One obeys a law of the type given in Eq. (23) and the second, showing less angular dependence,<sup>27,28</sup> is

$$P(\phi) \propto \cos^{3/2} \phi \quad (24)$$

These components have usually been termed quasi-specular and diffuse, respectively. The diffuse component has been attributed to structure on the surface comparable in dimension to the wavelength (e.g., boulders) which is capable of scattering into all angles. Since the diffuse component appears to be responsible for all the echo power for  $\phi > 50^\circ$  in the case of the moon<sup>27</sup> and  $\phi > 60^\circ$  for Venus,<sup>28</sup> it would be unreasonable to expect Eq. (23) to describe  $\bar{P}(\phi)$  for all  $\phi$  even neglecting absorption and refraction effects discussed above.

The parameter  $C$  is related to the mean surface slope,<sup>24</sup> and a number of workers have attempted to find values of this constant by matching the law to the experimental results. Different values are obtained if one first attempts to subtract out the diffuse component of the power. If this is neglected, then the value obtained is usually a lower estimate. In the case of Venus, however, the error should not be large since only  $\sim 10$  percent of the echo power is associated

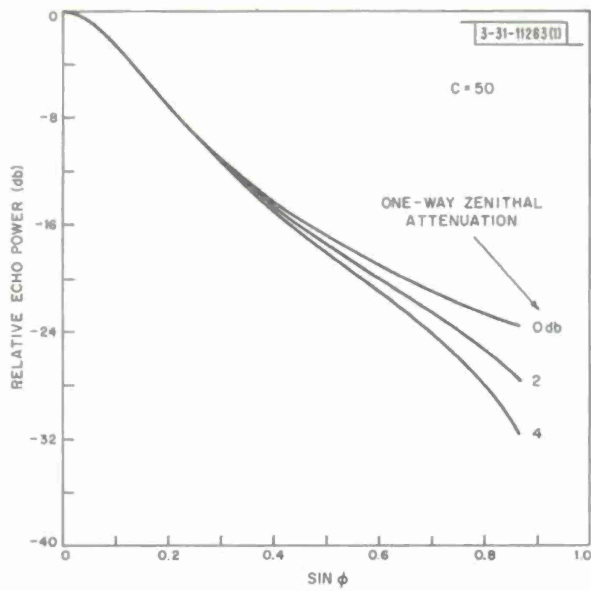
TABLE XI VALUES OF THE PARAMETER C				
$\lambda$ (cm)	Value of C (Moon)	References	Value of C (Venus)	References
600	165	29		
68	95	30	120	29
43			120	29
23	65	30	200	29
12.5			120	29
3.8	40	30	75	this paper

with this component. Table XI gives values of C for the moon and Venus neglecting the contribution of the diffuse component.

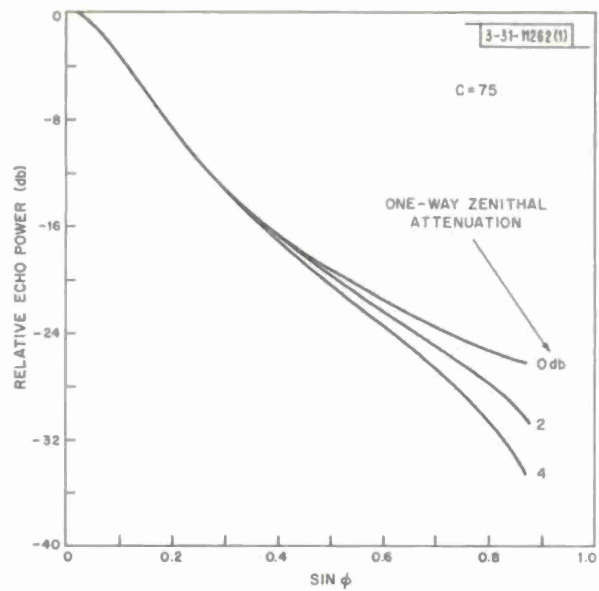
The value of  $C = 200$  at 23 cm for Venus is probably too high. The curve for  $\bar{P}(\phi)$  employed in this comparison was constructed by joining curves of  $\bar{P}(t)$  obtained with various pulse lengths.<sup>28</sup> Strongest and sharpest echoes probably weighted the mean near  $t \rightarrow 0$  to produce a more rapid fall-off than normally observed. On the other hand, the values obtained at the other wavelengths are probably lower limits because the resolution against Venus was in general poorer than for the 23-cm observations.<sup>28</sup> It is nevertheless evident that the value of the parameter C is higher for Venus than the moon at all wavelengths. Also, the value for Venus appears to be less dependent on wavelength to the accuracy of the present observations. We have therefore been interested in attempting to derive a value of C from the present observations. For this purpose we have computed theoretical curves of  $\bar{P}(\phi)$  according to Eq. (23) modified for the effects of atmospheric absorption as in Eq. (21), and compared these with the mean curve of Fig. 11. Figure 18(a-d) shows examples of such curves computed for various values of C and the one-way absorption. It can be seen that the absorption controls the behavior in the region  $\phi > 30^\circ$ , i.e., in a region where the theory is beginning to break down. It follows that this is not a reliable method by which to estimate the optical depth  $\tau$  [Eq. (21)]; however, it is also evident that the value of C derived should not be too sensitive to the assumed value of the absorption. Based upon this comparison we estimate that at 3.8 cm the appropriate value of C is  $\sim 75$ . The fit between the theory and experimental points is shown in Fig. 19. Thus there does appear to be a wavelength dependence in the average scattering properties of Venus and a crude relation between the moon and Venus is the supposition that  $C(\lambda)_{\text{moon}} = \frac{1}{2} C(\lambda)_{\text{Venus}}$ .

The relationship between C and the rms slope of the surface is far from straightforward.<sup>26,30</sup> There are difficulties associated with defining what is really meant by a slope when the surface is described by an exponential auto-correlation function and the horizontal scale over which the sampling is carried out is unknown. Thus in early papers (e.g., Ref. 31), a crude estimate of the rms surface slope was obtained from the parameter  $C = [d'\lambda/4\pi h_0^2]^2$  by somewhat arbitrarily setting  $\lambda = d'$ . When this is done for Venus, a mean slope of the order of  $5^\circ$  is obtained at  $\lambda \geq 23$  cm and  $\sim 6^\circ$  at  $\lambda = 3.8$  cm. Actually, as shown in Ref. 30 for the case of the moon, the horizontal scales of importance in determining the effective slope sampled by the wave extend down to the size of the wavelength; thus this approximation has perhaps some justification.

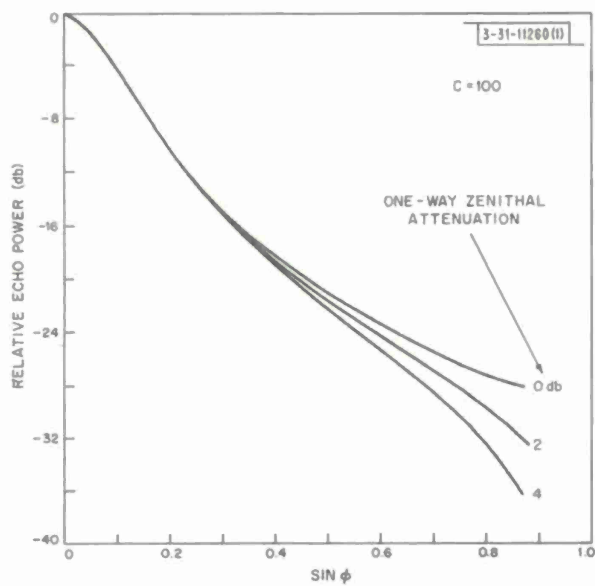




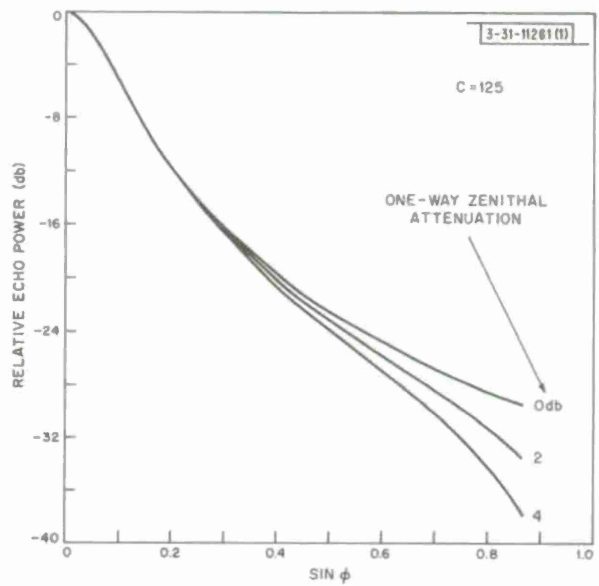
(a) Parameter  $C = 50$ .



(b) Parameter  $C = 75$ .



(c) Parameter  $C = 100$ .



(d) Parameter  $C = 125$ .

Fig. 18. Theoretical curves for angular scattering law according to Eq. (23) when effects of atmospheric absorption [Eq. (21)] are included.

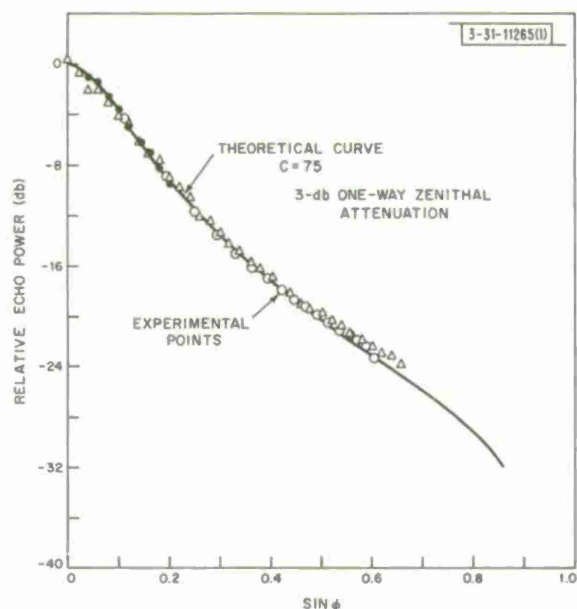


Fig. 19. Comparison of experimental data points shown in Fig. 11 with a theoretical curve (Fig. 18) for  $C = 75$  and 3-db one-way vertical attenuation.

However, it is also shown in that reference that the effective scale length changes with the angle of incidence  $\varphi$ . That is, the effect of the wavelength is to filter out certain components of the spectrum of surface roughness in a way which depends upon  $\varphi$ . Thus the ratio between the effective vertical and horizontal scales  $h$  and  $d'_e$  is approximately<sup>30</sup>

$$\frac{h_e}{d'_e} \approx \frac{\cos \varphi}{\sqrt{2C}} \quad (25)$$

The rms slope averaged over all possible directions over the surface  $\Theta_{\text{rms}}$  is  $\sqrt{2}h_e/d_e$ , thus

$$\Theta_{\text{rms}} \approx \frac{\cos \varphi}{\sqrt{C}}$$

Substitution into this expression of the values of  $C$  given in Table XI leads to rms slope estimates close to those cited above.

## VI. MAPPING OF ANOMALOUSLY SCATTERING REGIONS

### A. Introduction

As noted in the previous section, there appear to be regions on the disk of Venus that reflect radio waves markedly better than their environs. The locations of these anomalously bright features have been examined by workers at the Jet Propulsion Laboratory<sup>15,18,19</sup> and the Arecibo Ionospheric Observatory.<sup>32</sup> At JPL the existence of these regions has been evident from the appearance of "features" in the radio frequency power spectra. These features persist from day to day and are seen to move from high to low frequencies in a manner consistent with their being attached to a solid body in rotation. By determining the time history of the Doppler shift of each feature, both Goldstein<sup>18,19</sup> and Carpenter<sup>15</sup> have been able to locate some of the regions on the disk. In some cases, however, there is uncertainty in the position either because different features are seen to "blend"<sup>21</sup> or because the ambiguity between northern and southern hemispheres cannot be removed.

Spectra obtained at Haystack in 1966<sup>14</sup> at 3.8-cm wavelength displayed features similar to those observed by JPL.<sup>11,14</sup> (These provided one of several arguments that the 3.8-cm waves were indeed reaching the surface of Venus.)

The technique employed at Arecibo has been to divide the echo power both with respect to delay and frequency — so called range-Doppler mapping.<sup>21</sup> Since the delay defines an annulus on the projected disk, and the Doppler shift (in the absence of refraction) a line parallel to the projected apparent axis of rotation (see Fig. 14), the echo power associated with given delay and Doppler shift corresponds to the sum of the powers reflected from two regions, i.e., centered on  $(x, y)$  and  $(x, -y)$ . It follows that, if the projection of the apparent rotation axis changes with time, the power from a given region on the surface will be summed with that from a region in the opposite hemisphere which wanders over the disk. Thus the ambiguity associated with the identification of the hemisphere containing an isolated bright region may be removed (Fig. 20).

Neither technique described here permits an unambiguous map of the reflectivity to be obtained for the entire disk. For this reason the interferometer experiment outlined in Sec. I was conceived and carried out.<sup>1</sup> Unfortunately, the orientation of the baseline joining the two antenna systems employed in the interferometer measurements was somewhat unfavorable. When taken together with restrictions on the permitted hours of observation, this conspired to cause the synthesized antenna pattern to have large side-lobes. As a result, the best maps of the reflectivity variation were obtained by combining the interferometric resolution with delay Doppler mapping accomplished with the 500- $\mu$ sec coded pulse. From this work, eight anomalous regions were identified, four of which were considered reliable, and four somewhat uncertain. Five of these regions corresponded to features observed by JPL.

In this section we attempt to extend this work using the 60- $\mu$ sec coded pulse observations, and conclude with a discussion of the possible nature of these anomalously scattering regions.

## B. Short Coded Pulse Observations

### 1. Delay-Doppler Mapping

The technique of delay-Doppler radar mapping has been discussed elsewhere (for example, see Ref. 21), but in order to make this report generally self-sufficient, a brief discussion of the procedure is included here. Delay-Doppler mapping effectively permits the radar return from a set of transmitted coherent pulses or its equivalent demodulated pseudorandom coded signal

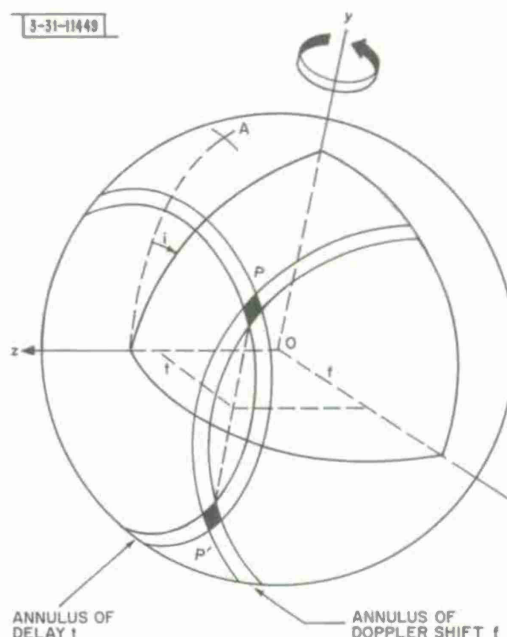


Fig. 20. Quadrant of hemisphere shown in Fig. 14 redrawn as part of whole sphere. Annuli of constant delay ( $t$ ) and Doppler shift ( $f$ ) are shown which instantaneously confine the received signals to those reflected from  $P$  and  $P'$ .

to be decomposed by spectral (that is Fourier series) analysis and range gating. When this is done all received elements of power are functions of two spatial coordinates on the body. In the case of a distant planet, these are annuli of constant delay and frequency as shown in Fig. 20. Unfortunately, with such a coordinate system there is an inherent ambiguity. As an example, it can be seen from Fig. 20 that elements P and P' in the upper and lower hemispheres, respectively, have the same delay and Doppler frequency coordinates. Therefore, if no other measures are taken, the information from the lower hemisphere is folded into the upper hemisphere and vice versa.

One approach to deriving information from the plots in the face of this ambiguity relies upon the fact that the orientation on the disk of the projected axis of rotation changes from day to day (Fig. 20), as does the position of the disk subradar point, so that in time different regions on the planet become conjugate to each other. Thus an isolated feature that has been properly identified as to hemisphere will remain fixed in planetary coordinates while an incorrect identification produces a coordinate location that appears to move from day to day. This technique requires that the Doppler axis orientation change considerably from day to day. In the case of Venus near inferior conjunction this condition is met only marginally as the maximum change in orientation over the period of observation is less than  $10^\circ$ .

## 2. Short-Coded Pulse Observations

Two types of coded pulse observations were carried out as outlined in Sec. III. The 500- $\mu$ sec pulse measurements were incorporated in the mapping analysis reported in Ref. 1. The short (60  $\mu$ sec) pulse observations were carried out primarily to provide accurate flight time estimates for the planet (Sec. III-D) and consequently only provided coverage of a small region at the center of the disk.

In these measurements a pseudorandom phase reversed code of 63 elements with a baud length of 60  $\mu$ sec was transmitted. The received signal was sampled in range delay at intervals of 30  $\mu$ sec. Only 32 of the possible 126 range boxes were demodulated and analyzed. For each of these 32 range boxes, 64 complex voltage samples spaced 15.120 msec apart were taken. The 64 Fourier series coefficients resulting from the spectral analysis of this time series were obtained yielding a spectral resolution of  $(64 \times 0.01512)^{-1} = 1.033$  Hz. An ensemble average of these coefficients was obtained over a block or series of blocks in any one day providing a complex two-dimensional delay-frequency data array of 64 frequencies by 32 delays. The power was obtained from the squared modulus of the complex coefficients.

Since there is a marked variation of brightness over the planetary disk owing to the intrinsic scattering law (Sec. V), it is necessary to convert the echo power vs delay and Doppler shift to a reflectivity map over the disk in a way which emphasizes the contrast between the anomalous regions and their environs. The steps in the data processing required to achieve this are:

- (a) A map consisting of the total power distributed in cells of range delay and Doppler frequency shift is obtained as described above.
- (b) An estimate of the system noise level is obtained by averaging the power in the delay-frequency cells preceding the planetary echo in range. This estimate of noise level is subtracted from the delay-frequency map values so that statistically the map represents an estimate of planetary echo power alone.



- (c) The echo power in each cell is divided by the area on the surface contributing power to its delay-frequency cell in order to obtain the power per unit area. In this way the effects of differences in the surface areas associated with the cells are removed (see p. 38).
- (d) Next, the effect of the mean surface slope is removed. This is done by dividing the power per unit area associated with each cell [obtained in step (c)] by the amount of power expected for that angle of incidence based upon an empirical scattering law.
- (e) These normalized values of brightness are next assigned to planetary positions and given spatial smoothing (see below).
- (f) Finally, the relative brightness vs position is displayed and photographed.

Conversion of the echo power per cell to echo power-per-unit projected area [i.e., step (c)] was achieved by dividing the power by the area associated with each delay-frequency cell given by

$$A = I(z_2, x_1, x_2) - I(z_1, x_1, x_2) \quad (26)$$

with

$$I(z, x_1, x_2) = \int_{x_1}^{x_2} \arcsin \sqrt{\frac{1-x^2-z^2}{1-x^2}} dx \quad (27a)$$

$$= \left[ x \arcsin \sqrt{\frac{1-x^2-z^2}{1-x^2}} - z \arcsin \frac{x}{\sqrt{1-z^2}} + \arcsin \frac{xz}{\sqrt{1-x^2} \sqrt{1-z^2}} \right]_{x_1}^{x_2} \quad (27b)$$

where

$$z_1 = z + \Delta z/2$$

$$z_2 = z - \Delta z/2$$

$z$  = direction cosine in delay direction of center of cell

$$\Delta z = c\Delta\tau/(2r_0)$$

$c$  = velocity of light

$\Delta\tau$  = transmitted pulse length (60  $\mu$ sec)

$r_0$  = planetary radius (6055 km)

$$x_1 = |x| - \Delta x/2$$

$$x_2 = |x| + \Delta x/2$$

$x$  = direction cosine in frequency direction of center of cell

$$\Delta x = \delta f/F_{CL}$$

$F_{CL}$  = center-to-limb Doppler

$$\delta f = 1.033 \text{ Hz.}$$



Scattering law compensation [step (d)] was applied through division of the data by an empirical planetary scattering law as a function of angle of incidence and hence range delay [Eq. (9)]. This procedure served to bring the mean power for each range ring to a nearly uniform level. The small planetary surface coverage of the data (about 10°) limited the range of intensities encountered thus obviating the need for a precise law. The actual law employed was that derived from the pulse data and shown in Fig. 10.

The echo power per unit projected area was converted from range and frequency coordinates to (ambiguous) positions on the planetary disk [step (e)] in the following way. Let  $r$  be the cell number in delay and  $d$  the cell number in frequency corresponding to planetary latitude and longitude  $\beta_i$  and  $\lambda_j$ . Let  $\sigma_o(r, d)$  be the normalized power density at  $r$  and  $d$ . Then the scattering function at  $\beta_i$  and  $\lambda_j$  is given by

$$S(\beta_i, \lambda_j) = \sigma_o(r, d) \quad (28)$$

where

$$r = [(1 - z_d)/(c\Delta t/2r_o)] + 1 \quad (29)$$

$$d = x_d/\Delta x + 1 + d_o$$

where

[ ] means the integral value

$d_o$  = frequency box corresponding to zero frequency

$$x_d = x_2 \cos \gamma + y_2 \sin \gamma$$

$$z_d = z_2$$

$$x_2 = \cos \beta_i \sin \lambda_j$$

$$y_2 = \sin \beta_i$$

$$z_2 = \cos \beta_i \cos \lambda_j$$

Some spatial smoothing was affected by subdividing the region around each planetary position  $(\beta_i, \lambda_j)$  into a  $3 \times 3$  lattice and forming the average over this neighborhood. In this way a  $101 \times 101$  matrix was developed in planetographic coordinates for display purposes.

A very precise programmable cathode ray oscilloscope was used in making the photographic maps. Since the display raster has many more programmable points than  $101 \times 101$ , the matrix was expanded into a  $1000 \times 1000$  matrix by a two dimensional interpolation routine that forms part of the display programs available in the computer. After the intensities were assigned one of 45 discrete levels, the film was exposed to each data point separately for a length of time linearly related to the power. In this way the photographs represent approximately the logarithm of the relative surface brightness (owing to the response of the film). Results for the region of the Doppler equator where the resolution is poor were omitted in photographic data presented here.

### 3. Results for the Short Coded Pulse

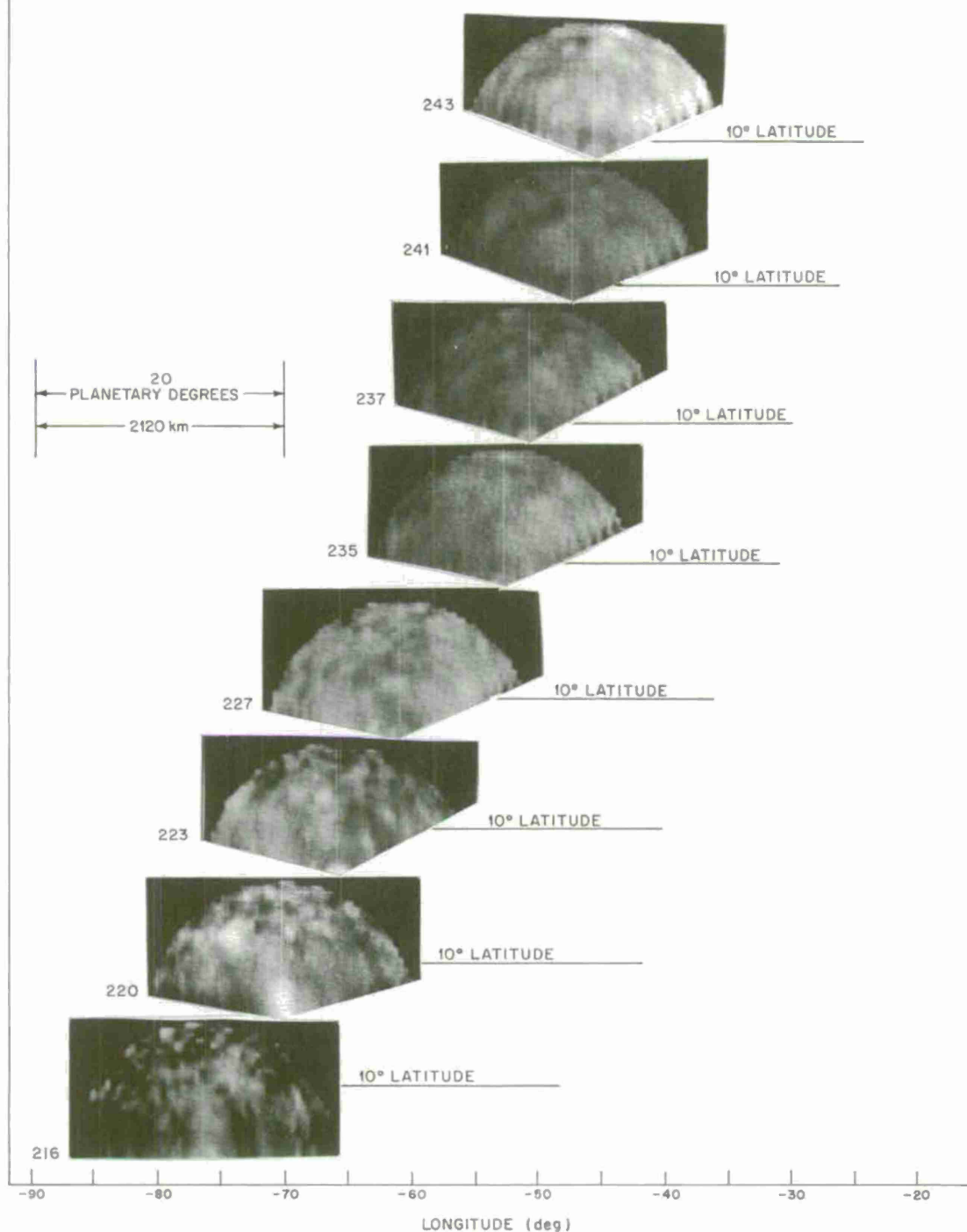
Figure 21 shows the results obtained in the manner outlined above for each of the days (indicated by number). The variation in reflectivity is presented as it would appear from the planetary pole. In Fig. 21(a) the power is presented as functions of longitude and latitude on the assumption that all the energy is returned from the Northern hemisphere, and in Fig. 21(b) on the assumption that only the Southern hemisphere contributes. The scale across the bottom of each figure shows the longitude and the sideways displacement of the plots illustrates the change in the subradar longitude with time. This method of presentation has been adopted because it forces genuine features to line up vertically through the plots. The best resolution obtained in these measurements is for regions lying along the Doppler axis at a point farthest from the subradar point. Table XII lists the resolution at this point in each of the runs, and Table XIII gives the latitude and longitude of the subradar point at the center time of the observations. As discussed earlier, ambiguity in the position of an isolated feature can in principle be resolved by noting the position for which it appears to be stationary in two or more photographs. However, because of the small change in the orientation of the Doppler axis encountered during these measurements, the identification of the hemisphere containing any feature is rather difficult. Nevertheless, there appear to be some distinguishable features in a series of photographs presented in Figs. 21(a) and (b). Figure 22 is a marked version of Fig. 21 showing schematically a tentative identification of several features, although the definite hemispheric assignment is not possible from these pictures alone.

Features reported by Goldstein have been designated by Greek letters  $\alpha, \beta, \dots \epsilon$ , and Carpenter has employed Roman letters with a figure suffix to indicate alternate possible locations of some features, e.g., D, D2, D3. In Ref. 4, reliable features were listed as Haystack I, II, ... and less reliable ones as Haystack A, B, C... In order to avoid introducing yet a new system, we have continued that employed in Ref. 4 and hence the one bona fide feature visible in Fig. 22 is listed as Haystack V. Other possible identifications are given in Table XIV. In addition to these bright features, there appears to be a dark region (denoted Z in Fig. 22) centered at  $\lambda = -67.5^\circ$  and  $\beta = -3.4^\circ$ .

#### C. Spectrum Observations

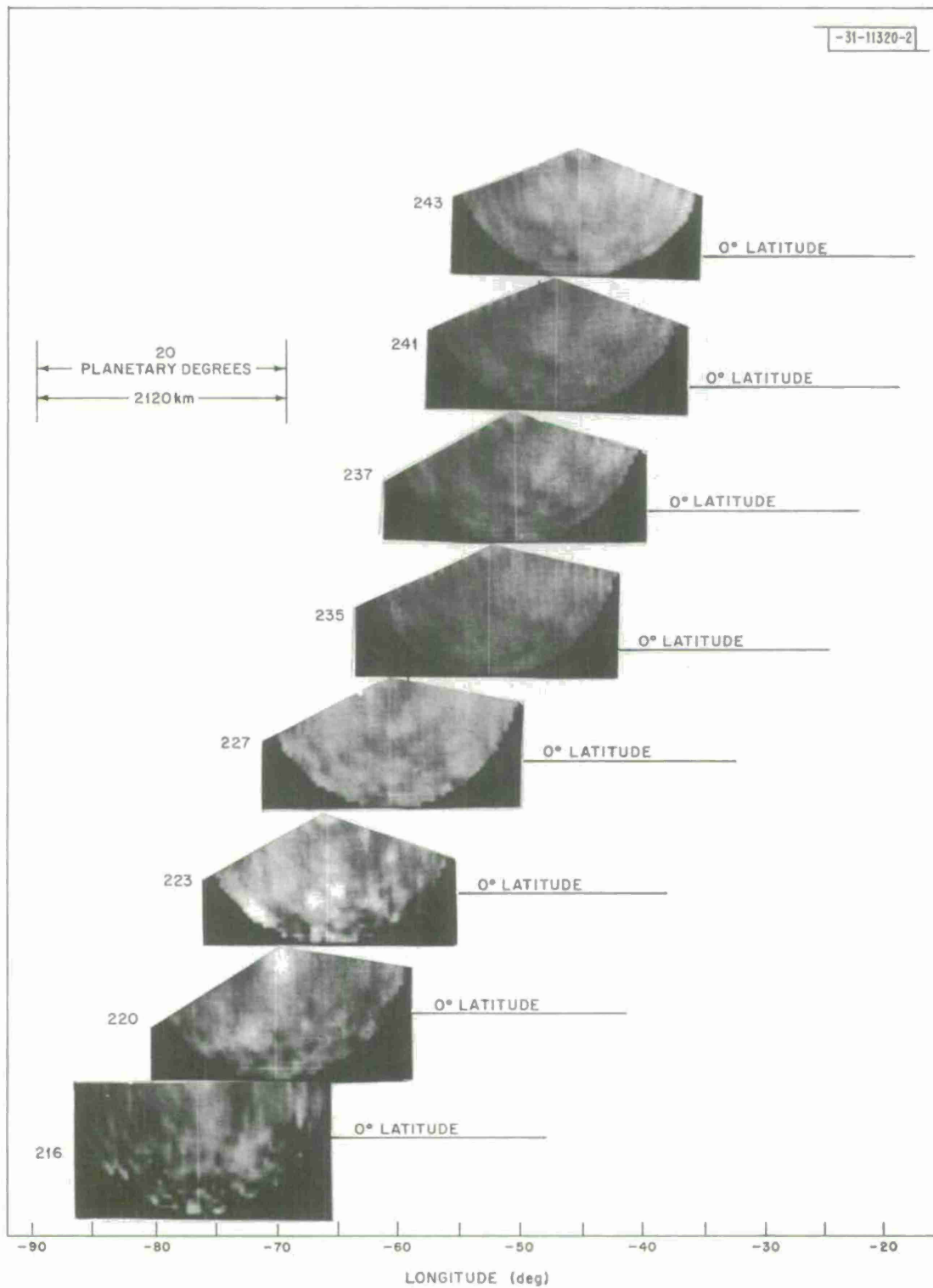
An attempt was made to supplement the results given in the previous section by examining the Hayford CW spectra for evidence of additional features. In order to do this the ratio of the power in the normalized spectrum  $P(f/f_{\max})$  averaged over each data block to that in the mean spectrum obtained for the entire set of observations was plotted. Figures 23(a-h) provide representative examples of these plots selected to be spaced at approximately weekly intervals. In each of these figures the original spectrum for the block is plotted below the ratio and it is evident in Figs. 23(a) to (c) that these are too noisy to permit anything meaningful to be obtained for the ratio in the region  $\pm 0.8 < f/f_{\max} \leq \pm 1.0$ .

We next computed the positions that the features identified in Ref. 4 and in the previous section would be expected to occupy and marked these on the ratio plots. Figures 23(a) to (h) show only the principal features Haystack I to V, the remainder having been omitted for the sake of clarity. Shown in the lower plots are the approximate positions of the features A through F listed by Carpenter.<sup>15</sup> It seemed evident from an inspection of this type that there are no major features in our observations that do not have some counterpart in those reported by JPL. We therefore discontinued efforts along these lines.



(a) Map assuming all power is reflected from northern hemisphere.

Fig. 21. Maps of reflectivity vs latitude and longitude for Venus obtained with 60- $\mu$ sec pulses.



(b) Map assuming all power is reflected from southern hemisphere.

Fig. 21. Continued.

TABLE XII RESOLUTION IN FREQUENCY AND RANGE DIRECTION ON THE DOPPLER AXIS AT A POINT* FARTHEST FROM SUBRADAR POINT†		
Day No.	Resolution in Frequency Direction (km)	Resolution in Delay Direction (km)
199	46.0	45
216	58.4	45
220	63.8	45
223	69.2	45
227	77.9	45
235	100.0	45
237	105.2	45
241	111.5	45
243	111.4	45
<p>* At an angle of incidence of 11.5°.</p> <p>† Though a range gate of 30 <math>\mu</math>sec was used, the resolution in range tabulated here corresponds to the baud length of 60 <math>\mu</math>sec.</p>		

TABLE XIII LONGITUDE AND LATITUDE OF SUBRADAR POINT FOR MAPS OF FIG. 21				
Day No.	Date (1967)	Approximate U.T. of Experiment	Subradar Position	
			Longitude (deg)	Latitude (deg)
216	4 Aug	1800	-76.6	4.3
220	8 Aug	2000	-70.2	5.2
223	11 Aug	1800	-65.9	5.8
227	15 Aug	1900	-61.0	6.7
235	23 Aug	1230	-52.8	8.0
237	25 Aug	1400	-50.9	8.2
241	29 Aug	1200	-47.4	8.5
243	31 Aug	1400	-45.7	8.6



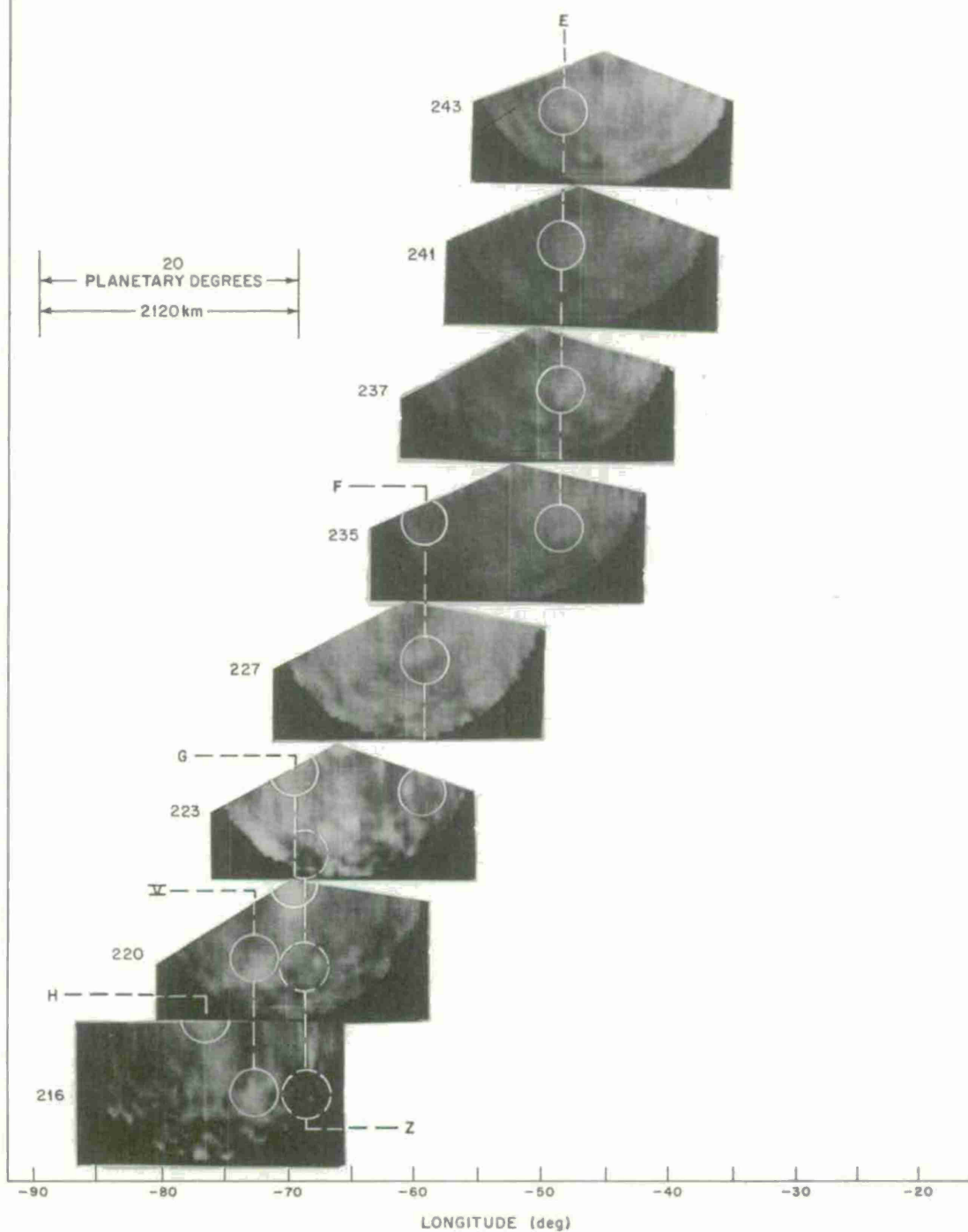


Fig. 22. Maps of reflectivity shown in Fig. 21(b) marked to show locations of features Haystack V (considered reliable) and Haystack E, F, G and H (considered probable).

TABLE XIV FEATURES OBSERVED IN THE 60- $\mu$ SEC CODED PULSE DELAY-DOPPLER MAPS		
Feature	Longitude (deg)	Latitude (deg)
RELIABLE Haystack V	$-73 \pm 1$	$-1.5 \pm 0.5$
PROBABLE Haystack E	$-49 \pm 1$	$+3 \pm 0.5$
Haystack F	$-61 \pm 1$	$+2 \pm 0.5$
Haystack G	$-70 \pm 1$	$+5 \pm 2$
Haystack H	$-77$	$+4 \pm 2$

#### D. Nature of the Features

A number of possible reasons can be advanced to explain the apparent brightness of the anomalously scattering regions. These include:

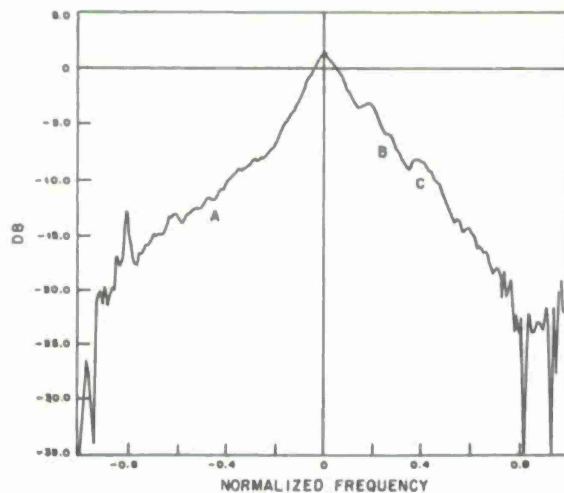
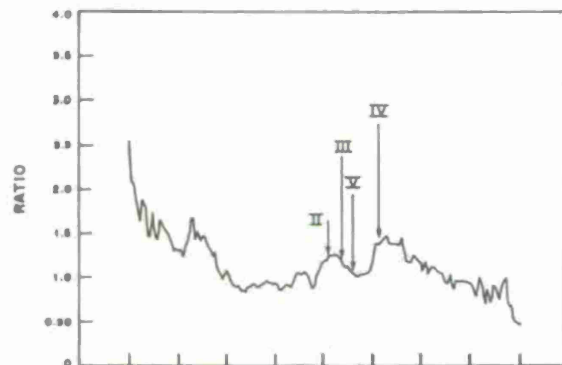
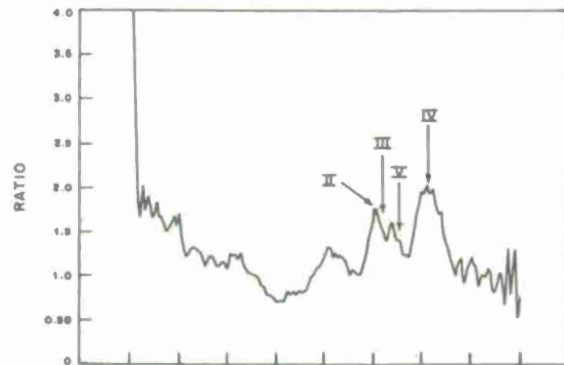
- (1) Differences in material – i.e., the intrinsic reflectivity is higher in these regions.
- (2) Differences in atmospheric absorption – i.e., these regions are higher (or perhaps hotter) than their environs. Since the attenuation in a  $\text{CO}_2$  atmosphere varies as  $P^2/T^{4.6}$ , where  $P$  is the pressure and  $T$  is temperature, this will result in a reduction of the atmospheric absorption above such regions.
- (3) Differences in surface roughness, the anomalously bright regions being rougher on average than their environs.

The variation of the relative brightness of the features with their position on the disk can serve to discriminate between some of these hypotheses. For example, a simple difference in reflectivity (1) should cause the same ratio of brightness between the region and its environs regardless of the distance of the feature from the subradar point. Mechanisms (2) and (3) would, however, be expected to cause the ratio to increase as the feature approaches the limb. This tendency is evident for several features marked in Fig. 23. Figure 24 shows the relative brightness for the peak of the complex region  $\beta$  (labelled II in our diagrams) as a function of  $|f/f_{\max}|$ . The brightness of this feature appears to increase linearly with distance from the center of the disk, regardless of direction. Also shown in Fig. 24 is the longitude of the feature measured along the equator from the subradar point. If atmospheric attenuation (2) were the mechanism, we would expect the enhancement to depend upon the secant of this angle – which is clearly not the case. It is arguable, however, that the blending of many features makes this plot unreliable since the blending changes with time [Figs. 23(a) to (h)]. Accordingly we have attempted a similar plot using the feature A of Carpenter's list. The enhancement ratio for this feature is plotted in Fig. 25. While the scatter of the points is large, it seems that the enhancement does not continue to increase as the feature approaches the limb.

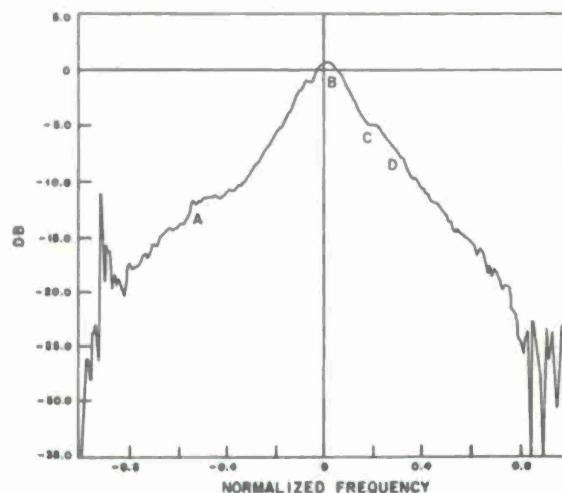
By this process of elimination, we conclude that a difference in roughness is probably the chief cause for the brightness of these regions with respect to their environs. A similar conclusion has been reached by JPL where it has been found that the features are brighter when

3-31-11450

3-31-11451



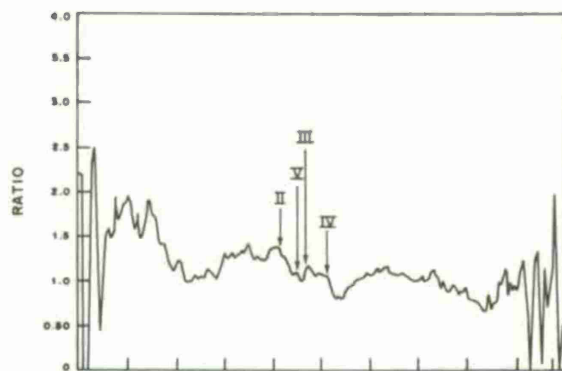
(a) Block No. 208-1.



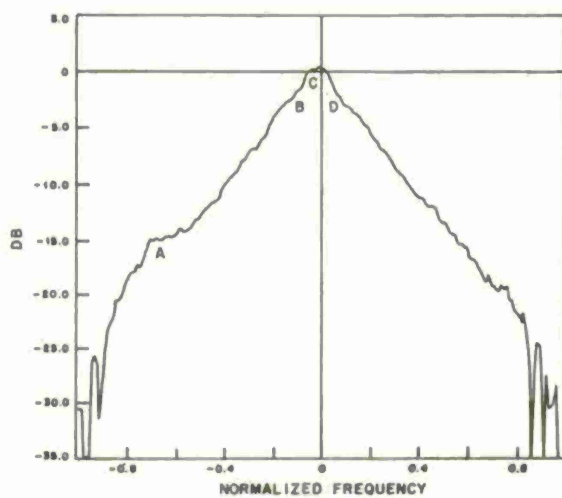
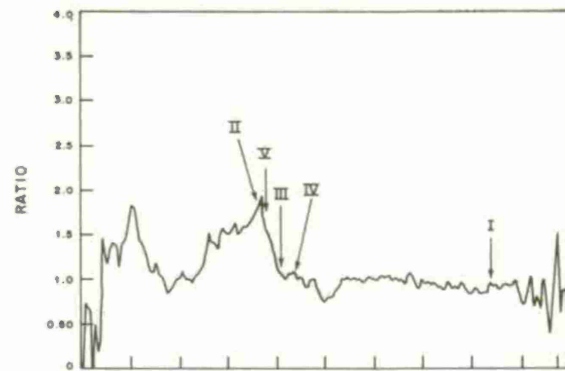
(b) Block No. 214-1.

Fig. 23(a-h). Bottom plot: Normalized echo power spectra  $\bar{P}(f/f_{\max})$  observed for data blocks obtained at approximately weekly intervals, showing positions expected for Carpenter's features A through F. Top plot: Ratio of power shown below to mean spectrum obtained by averaging all data blocks; expected locations of Haystack features I to V (Table XV) are shown.

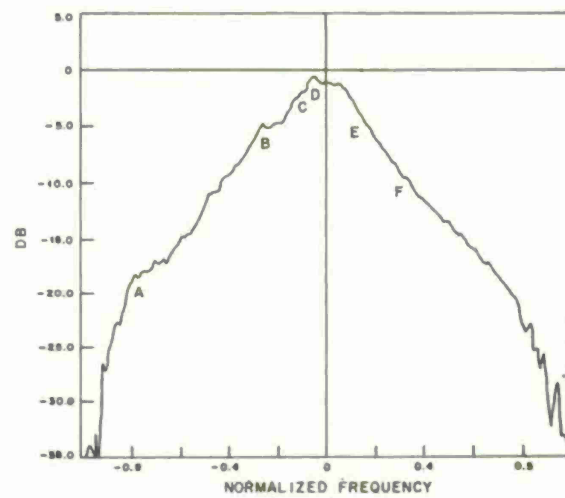
3-31-11452



3-31-11453



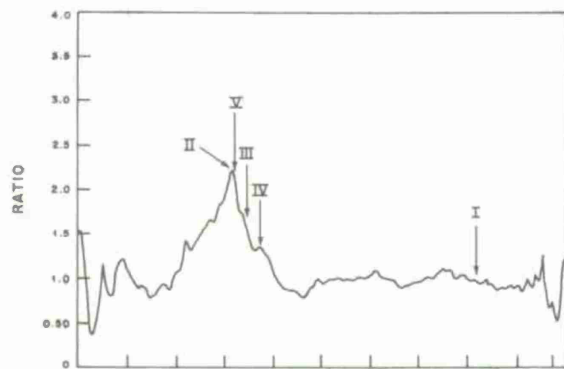
(c) Block No. 222-1.



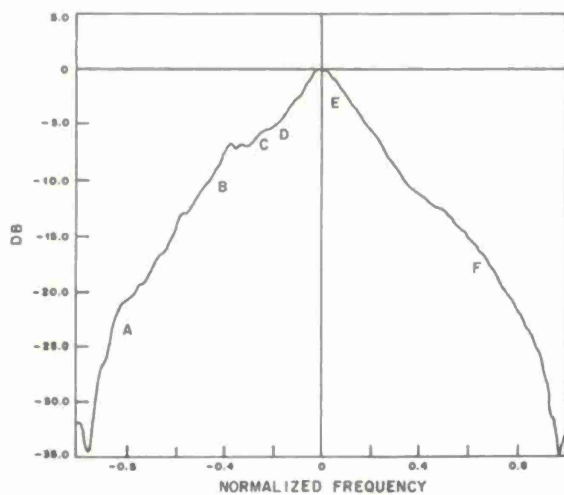
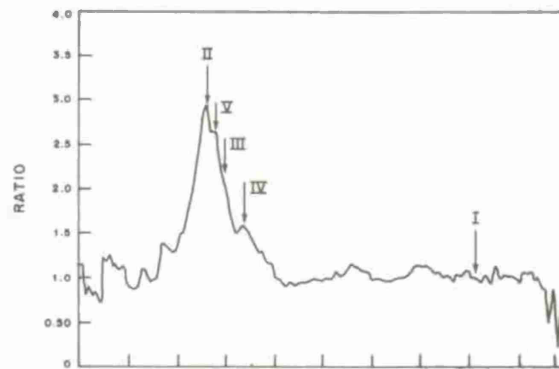
(d) Block No. 228-1.

Fig. 23(a-h). Continued.

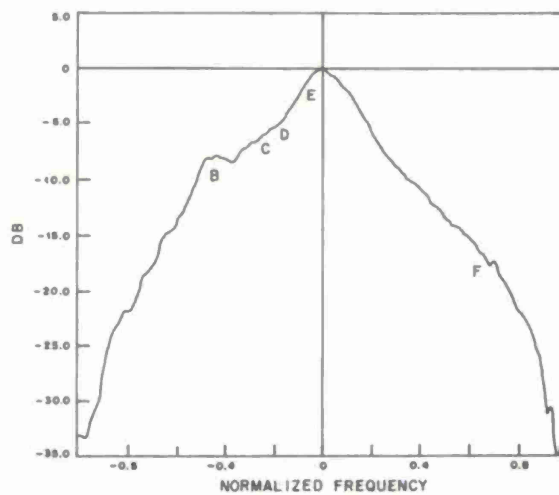
3-31-11454



3-31-11455



(e) Block No. 235-1.

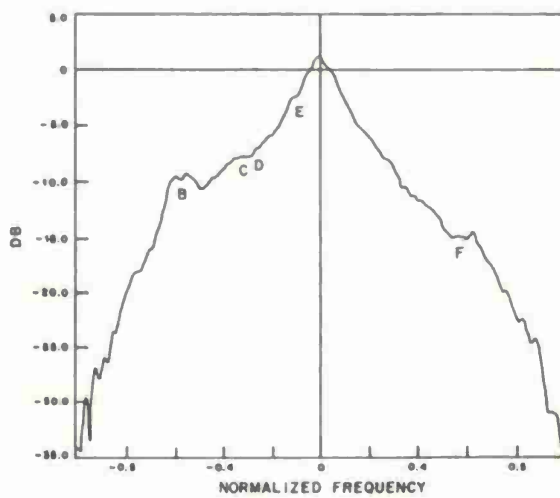
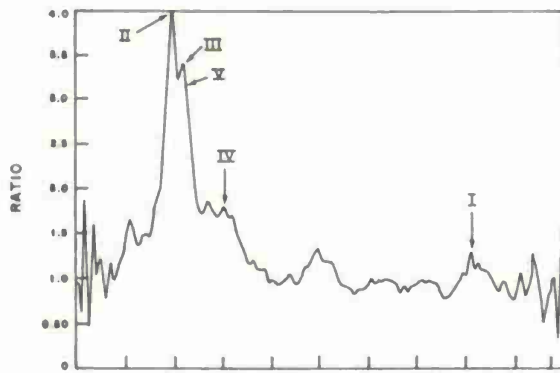


(f) Block No. 241-1.

Fig. 23(a-h). Continued.

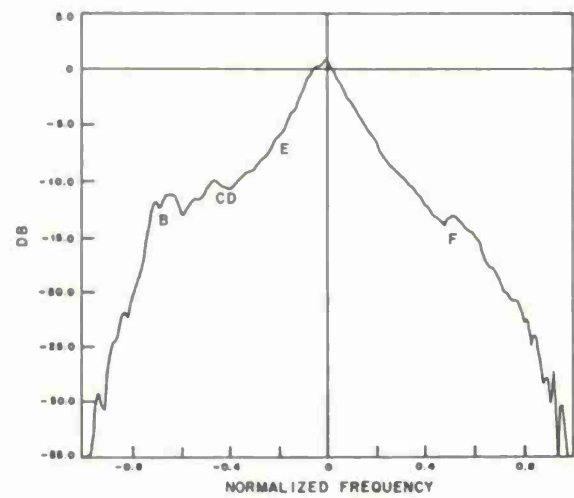
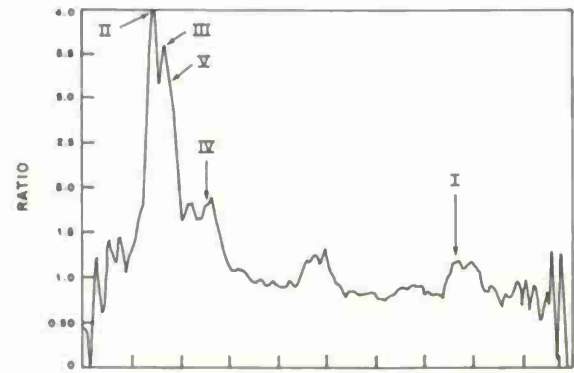


3-31-11456



(g) Block No. 249-1.

3-31-11457



(h) Block No. 256-1.

Fig. 23(a-h). Continued.

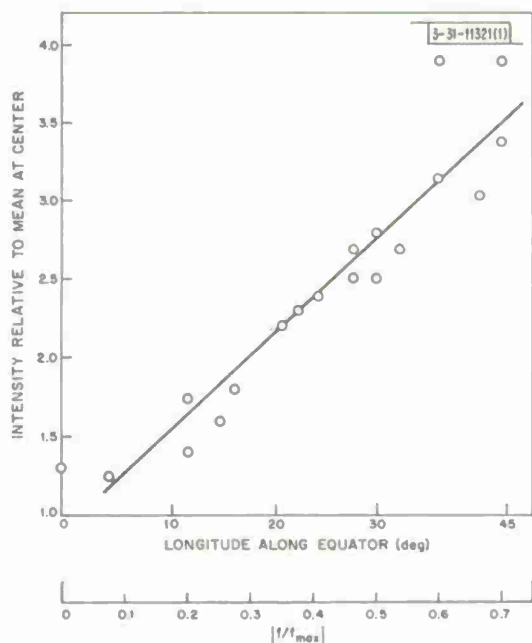


Fig. 24. Plot of relative intensity of complex region Haystack II as a function of position in ratio plots such as Figs. 23(a-h).

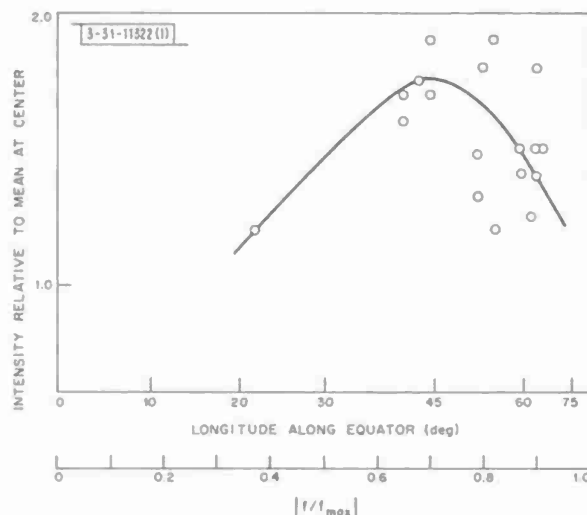


Fig. 25. Plot of the relative intensity of the isolated feature "Carpenter A" as a function of position in ratio plots such as Figs. 23(a-h).

examined in the depolarized component of the reflected signals than in the polarized (i.e., expected) sense. The fact that the features are readily detectable at 12.6-cm wavelength where the atmospheric attenuation is less (see Sec. V), may also be employed as an argument that height (or temperature) differences are not the prime physical effect. The features seen at 3.8 cm are brighter with respect to their environs than at 12.6 cm [cf. Fig. 23(h) with Fig. 12 of Ref. 15], but this could be due to increased effective roughness at the shorter wavelength.

The presence of rough regions on the surface should serve to raise the radar cross section owing to their greater backscattering capability except when they occupy the subradar region (where the smooth surface has a higher backscattering coefficient). Thus the dip in the cross section seen in Fig. 5 centered on day 225 may be associated with the passage of a number of features (Haystack G, IV, and V) through the vicinity of the subradar point at this time (see Table XIII).

### E. Discussion

Table XV summarizes the locations of the features found in these observations and those reported earlier.<sup>1</sup> The table also gives the probable correspondence of these features to those reported by JPL workers. Of those reported by Goldstein<sup>18,19</sup> none appear to be spurious, for though  $\gamma$  and  $\epsilon$  are not listed in Table XV, we have evidence of their existence from the 1966 results.<sup>11</sup> The feature  $\beta$  appears to be a large complex region which in our observations has been resolved into the centers listed as Haystack II and III.

Carpenter<sup>15</sup> has undertaken a more ambitious attempt to define feature locations on the disk. Of these, evidence of the existence of A through G was found in 1966,<sup>15</sup> though a determination of the exact locations of these from the 3.8-cm measurements was not attempted. We note that the Goldstein and Carpenter lists differ considerably. For example, Carpenter has no feature in

TABLE XV					
LOCATION OF RADAR FEATURES ON VENUS					
Features	Location from Haystack		Probable JPL Identification	Location from JPL	
	Longitude (deg)	Latitude (deg)		Longitude (deg)	Latitude (deg)
RELIABLE					
Haystack I	-1 ± 2	-26 ± 3	{ Goldstein α Carpenter F	0 ± ?	-29 ± 2
				0 ± 0.7	-26.7 ± 1.8
Haystack II	-81 ± 2	+24 ± 2	Goldstein β center =	-78 ± 6	±23 ± 4
Haystack III	-78 ± 2	+31 ± 2			
Haystack IV	-65 ± 3	-7 ± 3	Carpenter C	-68.9 ± 1.3	-6.8 ± 5.8
Haystack V	-73 ± 1	-1.5 ± 0.5	Carpenter C2	-70.0 ± 0.7	-2.5 ± 3.7
PROBABLE					
Haystack A	-68 ± 2	+23 ± 2	{ Carpenter D2 Goldstein δ	-70.0 ± 0.7	+22.7 ± 1.7
				-69 ± ?	+26 ± ?
Haystack B	-81 ± 3	-12 ± 3	Carpenter B1	-75.8 ± 0.6	-11.9 ± 4.4
Haystack C	-36 ± 3	-13 ± 2	None		
Haystack D	-39 ± 4	+10 ± 4	None		
Haystack E	-49 ± 1	+3 ± 0.5	Carpenter E	-49.3 ± 0.9	+6.4 ± 8.5
Haystack F	-61 ± 1	+2 ± 0.5	{ Carpenter D Carpenter D3	-61.0 ± 1.8	-1.7 ± 7.1
				-60.5 ± 0.7	-2.5 ± 4.1
Haystack G	-70 ± 1	+5 ± 2	None		
Haystack H	-77 ± 1	+4 ± 2	Carpenter B	-78.1 ± 2.6	-3.3 ± 8.7

the location of  $\beta$  though his paper implies that B, C and D of his list are the same feature. Similarly, Goldstein's map has no feature in the region centered on  $-70^\circ$  longitude  $-5^\circ$  latitude where a large number of Carpenter's features lie. It appears that this region is a second complex reflecting area, which in our measurements has been resolved into Haystack IV and V with the possible addition of Haystack B, F and H. In this general vicinity, Carpenter lists B, B1, C, C2, D (and D3), all of which appear to have some counterpart in the Haystack observations. Indeed, the only feature in Carpenter's map that was not recognized in our observations is the feature C1 which Carpenter regards as a tentative identification.

In summary, the work reported here confirms and extends somewhat earlier observations at JPL of the location of anomalously reflecting regions on the disk of Venus. Using the coordinate system defined in Sec. IV, the largest regions of anomalous reflectivity are centered at approximately  $-80^\circ$  longitude  $26^\circ$  latitude and  $-70^\circ$  longitude  $-5^\circ$  latitude. Each of these extends over a region of the order of  $10^\circ \times 10^\circ$ , and appears to contain a number of centers. Since these two features tend to lie at the same Doppler shift, it is difficult to separate them using Doppler and/or delay-Doppler resolution alone, and the interferometer measurements reported in Ref. 1 represent a considerable advance. Nevertheless, some misidentification may have

been made, and in any event it seems doubtful that these regions have been fully resolved. When this is done, it is likely that their complexity will lead to the abandonment of the idea of locating individual features. Elsewhere on the disk there are isolated regions of high reflectivity that have not been resolved in the measurements made thus far.

It is suggested that the principal difference between the anomalously bright regions and their environs is that they are rougher on a scale comparable with the wavelength. A reason for such differences is not known. Possibly these features are of external origin (e.g., impact craters) though internal effects (e.g., convection cells) may be capable of giving rise to differences in surface roughness.

#### ACKNOWLEDGMENTS

The authors are indebted to T. Hagfors for permitting the measurements reported here to be taken during experiments which he conducted to map the radar brightness distribution of Venus. Results of these experiments have been reported elsewhere. Many members of the Haystack Microwave Facility -- particularly M. Leavy and R.R. Silva -- made valuable contributions to the conduction and interpretation of the experiments reported here. The interest and encouragement of P.B. Sebring, M.L. Stone and T. Hagfors are gratefully acknowledged, as is the invaluable assistance of I.I. Shapiro and his colleagues who prepared the radar ephemerides.

## REFERENCES

1. A. E. E. Rogers, T. Hagfors, R. A. Brockelman, R. P. Ingalls, J. I. Levine, G. H. Pettengill, and F. S. Weinstein, "A Radar Interferometer Study of Venus at 3.8 cm," Technical Report 444, Lincoln Laboratory, M.I.T. (14 February 1968), DDC 670167.
2. T. Hagfors, G. H. Pettengill, and A. E. E. Rogers, "Radar Interferometer Observations of Venus at 3.8 cm," presented at Spring URSI Meeting, Washington, D. C., 1968.
3. I. I. Shapiro, G. H. Pettengill, M. E. Ash, M. L. Stone, W. B. Smith, R. P. Ingalls, and R. A. Brockelman, "Fourth Test of General Relativity: Preliminary Results," *Phys. Rev. Letters* 20, 1265 (1968).
4. H. G. Weiss, "The Haystack Microwave Research Facility," *IEEE Spectrum* 2, 50 (1965), DDC 614734.
5. B. E. Nichols and D. Karp, "Westford Radar and Microwave Equipment," *Proc. IEEE* 52, 576 (1964).
6. H. E. Frachtman, "Haystack Pointing System: Planet," Group Report 1964-46, Lincoln Laboratory, M.I.T. (10 September 1964), DDC 606501.
7. J. V. Evans, "Modulation, Demodulation and Data Processing," in *Radar Astronomy*, edited by J. V. Evans and T. Hagfors (McGraw-Hill, New York, 1968), Chap. 9.
8. N. N. Brenner, "Three Fortran Programs that Perform the Cooley-Tukey Fourier Transform," Technical Note 1967-2, Lincoln Laboratory, M.I.T. (28 July 1967), DDC 657019.
9. J. W. Cooley and J. W. Tukey, "An Algorithm for the Machine Calculation of Complex Fourier Series," *Mathematics of Computation* 19, 297 (1965).
10. R. J. Allen, "Observation of Several Discrete Radio Sources at 3.64 and 1.94 Centimeters," Ph.D. Thesis, Elec. Eng. Dept., M.I.T. (January 1967).
11. J. V. Evans, "Variations in the Radar Cross Section of Venus," *Astron. J.* 73, 125 (1968).
12. B. R. Bean and E. J. Dutton, *Radio Meteorology* (U.S. Govt. Printing Office, Washington, D. C., 1966), Chap. 7.
13. M. A. Gordon, private communication.
14. J. V. Evans, R. P. Ingalls, L. P. Rainville, and R. R. Silva, "Radar Observations of Venus at 3.8 cm Wavelength," *Astron. J.* 71, 902 (1966).
15. R. L. Carpenter, "Study of Venus by CW Radar - 1964 Results," *Astron. J.* 71, 142-52 (1966).
16. D. Karp, W. E. Morrow, Jr., and W. B. Smith, "Radar Observations of Venus at 3.6 cm," *Icarus* 3, 473 (1964).
17. I. I. Shapiro, "Resonance Rotation of Venus," *Science* 157, 423 (1967).
18. R. M. Goldstein, "Preliminary Venus Radar Results," *J. Research Natl. Bur. Standards* 69D, 1623 (1965).
19. R. M. Goldstein, "Radar Studies of Venus," in *Moon and Planets*, edited by A. Dollfus (North Holland Publ. Co., Amsterdam, 1967), p. 126.
20. D. O. Muhleman, "Radar Scattering of Venus and Mercury at 12.5 cm," *J. Research Natl. Bur. Standards* 69D, 1630 (1965).
21. P. E. Green, "Radar Measurements of Target Scattering Properties," in *Radar Astronomy*, edited by J. V. Evans and T. Hagfors (McGraw-Hill, New York, 1968), Chap. 1.
22. R. M. Goldstein, "Venus Characteristics by Earth-Based Radar," *Astron. J.* 69, 12 (1964).
23. R. L. Carpenter, "Study of Venus by CW Radar," *Astron. J.* 69, 2 (1964).
24. B. R. Bean and E. J. Dutton, *Radio Meteorology* (U.S. Govt. Printing Office, Washington, D. C., 1966), Chap. 3.
25. R. A. Phinney and D. L. Anderson, "On the Radio Occultation Method for Studying Planetary Atmospheres," *J. Geophys. Res.* 73, 1819 (1968).



26. T. Hagfors, "Backscattering from an Undulating Surface with Applications to Radar Returns from the Moon," *J. Geophys. Res.* 69, 3779 (1964); see also Radar Astronomy (McGraw-Hill, New York, 1968), Chap. 4.
27. J. V. Evans, "Radar Studies of the Moon," *Radio Science* 69D, 1637 (1965); see also Radar Astronomy (McGraw-Hill, New York, 1968), Chap. 5.
28. J. V. Evans, R. A. Brockelman, R. C. Henry, G. M. Hyde, L. G. Kraft, W. A. Reid, and W. W. Smith, "Radio Echo Observations of Venus and Mercury at 23 cm Wavelength," *Astron. J.* 70, 486 (1965).
29. P. Beckmann and W. K. Klemperer, "Interpretation of the Angular Dependence of Backscattering from the Moon and Venus," *Radio Science Natl. Bur. Standards* 69D, 1669 (1965).
30. "Radar Studies of the Moon," Final Report, Vol. I, Lincoln Laboratory, M.I.T. (31 August 1967).
31. J. V. Evans and G. H. Pettengill, "The Scattering Behavior of the Moon at Wavelengths of 3.6, 68 and 784 Centimeters," *J. Geophys. Res.* 68, 423 (1963).
32. R. F. Jurgens, private communication.

DOCUMENT CONTROL DATA - R&D		
(Security classification of title, body of abstract and indexing annotation must be entered when the overall report is classified)		
1. ORIGINATING ACTIVITY (Corporate author)  Lincoln Laboratory, M.I.T.		2a. REPORT SECURITY CLASSIFICATION Unclassified  2b. GROUP None
3. REPORT TITLE  Reflection Properties of Venus at 3.8 cm		
4. DESCRIPTIVE NOTES (Type of report and inclusive dates) Technical Report		
5. AUTHOR(S) (Last name, first name, initial)  Ingalls, Richard P.                      Levine, James I.                      Rogers, Alan E. Brockelman, Richard A.              Pettengill, Gordon H.              Weinstein, Franklin S. Evans, John V.                      Rainville, Louis P.		
6. REPORT DATE 6 September 1968	7a. TOTAL NO. OF PAGES 60	7b. NO. OF REFS 32
8a. CONTRACT OR GRANT NO. AF 19 (628)-5167 b. PROJECT NO. 649L c. d.	9a. ORIGINATOR'S REPORT NUMBER(S) Technical Report 456  9b. OTHER REPORT NO(S) (Any other numbers that may be assigned this report) ESD-TR-68-262	
10. AVAILABILITY/LIMITATION NOTICES  This document has been approved for public release and sale; its distribution is unlimited.		
11. SUPPLEMENTARY NOTES  None	12. SPONSORING MILITARY ACTIVITY  Air Force Systems Command, USAF	
13. ABSTRACT  During the fall of 1967, the M.I.T. Lincoln Laboratory Haystack radar was employed to study the scattering properties of the planet Venus at 3.8-cm wavelength. An increase in the transmitter power to 300 kW CW and a reduction in the system noise temperature to 60°K provided a considerable improvement in the radar performance compared with that available for earlier measurements. The frequency power spectra of the echoes were determined by digital Fourier analysis of the received signals. The total power in each spectrum was computed to yield the value for the radar cross section of Venus. These average 1.75 percent of the projected area of the disk, in good agreement with a reanalysis of results obtained in 1966. The signal spectra have been averaged and employed to derive the angular scattering dependence $P(\phi)$ for waves reflected from a region near the center of the disk ( $0 < \phi < 60^\circ$ ), where atmospheric refraction effects seem likely to be small. Comparison of this law with a law derived from similar measurements at 12.5-cm wavelength performed at the Jet Propulsion Laboratory (JPL) shows limb darkening, which is attributed to atmospheric absorption of the shorter wavelength signals. From the amount of limb darkening, the difference in the two-way atmospheric absorption at the two wavelengths is estimated to be $5 \pm 1$ db. The radar cross section observed at 3.8 cm is lower than that at 12.5 cm by $8 \pm 3$ db. Thus it is concluded that the one-way absorption of 3.8-cm microwaves by the atmosphere of Venus is at least 2.5 db and possibly more. This is significantly greater than can be accounted for by the recent U.S. and Soviet probe experiments, which imply an atmosphere of CO <sub>2</sub> with surface pressure of 20 atmospheres. Either the pressure is considerably greater than this or other gases that are more effective microwave absorbers are present. The scattering behavior of the disk center, i.e., in a region where atmospheric refraction and absorption have not significantly altered the shape of the scattering law, has been compared with that at other wavelengths. It is concluded that Venus, like the moon, appears to be rougher at centimeter wavelengths than meter or decimeter wavelengths. However, for scales important in these measurements, i.e., over horizontal distances of the order of a few times the wavelength, the rms slopes found for Venus are of the order of $1/\sqrt{2}$ times those found for the moon. Delay-Doppler mapping experiments are reported which yielded a resolution of $\sim 100 \times 100$ km. These show the existence of bright features and the locations of these are tabulated. The report closes with a discussion of the nature of these features. It is concluded that many, if not all, are rougher and denser than their environs and, in view of the general smoothness found elsewhere, are possibly young features.		
14. KEY WORDS  radar astronomy                      radar cross section                      atmospheric absorption scattering                      angular scattering dependence              pressure Venus                      atmospheric refraction              rms slopes 3.8-cm wavelength              limb darkening              delay-Doppler mapping		



